The Canadian Journal of Mineralogy and Petrology
ISSN 2817-1713
Vol. 61, pp. 927-964 (2023)
DOI: 10.3749/2300008

GENESIS AND NEW MINERAL CHEMISTRY DATA OF CARLOSBARBOSAITE, A POTENTIAL U AND Nb ORE SOURCE FROM MIAROLITIC-, A-TYPE GRANITES AND NYF PEGMATITES OF THE LA CHINCHILLA PLUTON, VELASCO RANGES, LA RIOJA, ARGENTINA

RAÚL LIRA[§]

Museo de Mineralogía y Geología "Dr. Alfred W. Stelzner", FCEFyN, Universidad Nacional de Córdoba. Av. Vélez Sarsfield 249, X5000JJC, Córdoba, Argentina
Consejo Nacional de Investigaciones Científicas y Técnicas (CONICET), Av. Vélez Sarsfield 249, X5000JJC, Córdoba, Argentina

FRANCISCO J. PARRA

Comisión Nacional de Energía Atómica, Subgerencia Regional Centro. Espinel 902, X5001BKW, Córdoba, Argentina

MARCO E. BIGLIA

Museo de Mineralogía y Geología "Dr. Alfred W. Stelzner", FCEFyN, Universidad Nacional de Córdoba. Av. Vélez Sarsfield 249, X5000JJC, Córdoba, Argentina

ORQUÍDEA MORELLO

Comisión Nacional de Energía Atómica. Av. del Libertador 8250, (1429) Ciudad Autónoma de Buenos Aires, Argentina

ALINA B. GUERESCHI

Departamento de Geología Básica (Facultad de Ciencias Exactas, Físicas y Naturales, Universidad Nacional de Córdoba) and Centro de Investigaciones en Ciencias de la Tierra (CONICET - Universidad Nacional de Córdoba). Av. Vélez Sársfield 1611, X5016GCA, Córdoba, Argentina

ABSTRACT

The La Chinchilla granite is a ~3.75 km^2 epizonal pluton of Lower Carboniferous age located in Sierra de Velasco, Sierras Pampeanas, Argentina. Equigranular micropegmatitic and porphyritic main granite types host abundant millimeter- to <2 m-sized miarolitic pegmatites and pockets of simple major mineralogy (±beryl). Both granite types host micrometer-sized accessory species [*i.e.*, monazite-(Ce), several high field strength element oxide species, ilmenite, cassiterite, fluorapatite] and fluorite. A F-Na-rich fluid phase promoted strong albitization at late-miarolitic stages, along with crystallization of extremely F-rich polylithionite and fluorite, and the formation of replacing pyrochlore group species associated with a second generation of cassiterite. The increase of the Ta# from hydroxycalciopyrochlore to hydroxycalciomicrolite and from micromiarolitic cassiterite (cassiterite 1) to hydrothermal cassiterite (cassiterite 2) supports Nb-Ta fractionation at hydrothermal temperatures. Carlosbarbosaite $[(UO_2)_2Nb_2O_6(OH)_2 \cdot 2H_2O]$ occurs as a pseudomorphic or short-range transported phase. Low-*T*, hydrothermal carlosbarbosaite formed after the replacement of columbite-(Fe), U-free Nb-bearing ilmenite, and likely after U-bearing pyrochlore supergroup species and a columbite group mineral, plausibly due to interaction with a hydrothermal, U^{6+}(±Nb±Ta)-enriched fluid, in some cases a SiO_2-bearing fluid. This fluid likely represents a lower *T*, less alkaline, and more oxidizing fluid that evolved from the higher *T* F-Na-rich fluids active during the late-miarolitic hydrothermal stage. Low-*T*, hydrothermal carlosbarbosaite has the ideal U-,Nb-rich endmember composition, though it is significantly richer in Ca and poorer in total Nb+Ta but with higher Nb# than that from the type

[§] *Corresponding author e-mail address*: raul.lira@unc.edu.ar

locality. Supergene fluids deposited the transported type, which attained economic concentrations in a fault zone where restricted, likely alkaline oxidizing conditions could have favored Nb mobility.

Keywords: carlosbarbosaite, A-type granite, NYF miarolitic pegmatites, fluorine-rich, niobium mobility, uranium.

Introduction

The La Chinchilla granite is located in Sierra de Velasco (Pampean Ranges), La Rioja province of northwestern Argentina. The La Chinchilla pluton is an outstanding example of epizonal calcalkaline magmatism of highly specialized chemistry. Since its early description by Grosse *et al*. (2005), it has already been studied by several authors, mostly focused on petrological data, emplacement conditions, and alteration-mineralization aspects (*e.g.*, Grosse *et al*. 2009, Dahlquist *et al*. 2010, Salvatore *et al*. 2013, Macchioli Grande *et al*. 2015, 2019, Bardelli *et al*. 2018). This pluton became a significant exploration target of the National Atomic Energy Commission of Argentina (CNEA) due to its highly anomalous U contents (López *et al.* 2020), mainly in the form of local concentrations of supergenic carlosbarbosaite, a rare secondary hydrated uranyl niobate of formula $(UO_2)_2Nb_2O_6(OH)_2{\cdot}2H_2O$. Since discovery, ~1500 m of core drilling (some holes down to 300 m deep) and other complementary exploration work and studies have been done to evaluate the potential of U mineralization; a speculative resource estimated in the equigranular granite facies indicated ~990 t of U at an average grade of 0.0159 wt.% U (Urquiza 2011, CNEA, unpublished report). Since 2015, hundreds of miarolitic pegmatite bodies with ubiquitous smoky quartz and sporadic amazonite and beryl have been observed widespread throughout the La Chinchilla body and were classified as NYF family and miarolitic class (Lira *et al*. 2015).

The main goal of this contribution is to provide new mineral chemistry data and detailed evidence about the origin of carlosbarbosaite, including a discussion of the low-*T* mobility of Nb. The U solubility is also considered, highlighting the potentiality of carlsobarbosaite as both a U and Nb ore source when appropriate precipitation conditions are met. In addition, a characterization of micromiarolitic and miarolitic pegmatites and their host granites is provided, and their mineral chemistry evolution is interpreted, as a background for a better understanding of the geological environment where carlosbarbosaite is formed.

Geological Background

La Chinchilla granite

The La Chinchilla leucomonzogranite is located in the Sierra de Velasco, northwest of La Rioja city (Fig. 1a), within the largest outcropping area of plutonic rocks of the Sierras Pampeanas (Toselli *et al.* 1996). The magmatic units of Sierra de Velasco are, in the vast majority, peraluminous deformed granites of Ordovician age related to the Famatinian orogeny (*e.g.*, Pankhurst *et al.* 2000). These largely well-exposed granites have been locally intruded by several scattered, smaller plutons of Devonian to Lower Carboniferous age (*e.g.*, Dahlquist *et al.* 2010). Due to their geographical proximity and spatial association with La Chinchilla, the other two plutons of this group, the Sanagasta and Huaco granites, are also considered (Grosse & Sardi 2005, Grosse *et al.* 2009, Fig. 1a).

The inequigranular porphyritic Huaco granite extends over 620 km^2 (Grosse & Sardi 2005). It varies in composition from syenogranite to monzogranite with an alkali-calcic to slightly calc-alkaline and moderately peraluminous chemistry (Grosse 2007). The crystallization age estimates of the host Huaco granite range from 353 ± 1 Ma (chemical U/Pb in monazite, Grosse *et al.* 2009) to 357 ± 3 Ma (U/Pb LA-ICP-MS in zircon, Dahlquist *et al.* 2013). The La Chinchilla pluton is a small (~3.75 km^2), oval-shaped, ESE-stretched body that intrudes the Huaco granite (Fig. 1b). A U/Pb age on monazite yielded an age of 344.5 ± 1.4 Ma (Grosse *et al.* 2009). Its composition varies from syenogranite to monzogranite. The equigranular facies described by Grosse *et al*. (2009) is composed of quartz (37–42%), $albite_{An1-2}$ (25–33%), perthitic microcline (19–34%), "zinnwaldite" and protolithionite (4–9%), up to 1% fluorite, and lesser amounts of zircon, monazite, opaque phases, apatite, and, occasionally, beryl. We use the term "protolithionite" as done by Grosse *et al.* (2009) to refer to a Li mica member that forms a series of increasing Li from siderophyllite, as widely published by Tischendor *et al.* (2004) and previous publications on the subject in their classification scheme using the mgli-feal chemical parameters. Subsequent work by Salvatore *et al*. (2013) led to the identification of four main monzogranite facies in the La Chinchilla pluton (Fig. 1b). Arranged according to decreasing outcropping surface, these are (1) Porphyritic facies (coarse groundmass), (2) Equigranular facies, (3) Porphyritic facies (fine groundmass), and (4) Fine-grained (aplitic) border zone facies (*i.e.*, microgranite). The La Chinchilla granite displays a rich primary and secondary accessory mineralogy; Cuney (*pers. commun.* 2013) described the

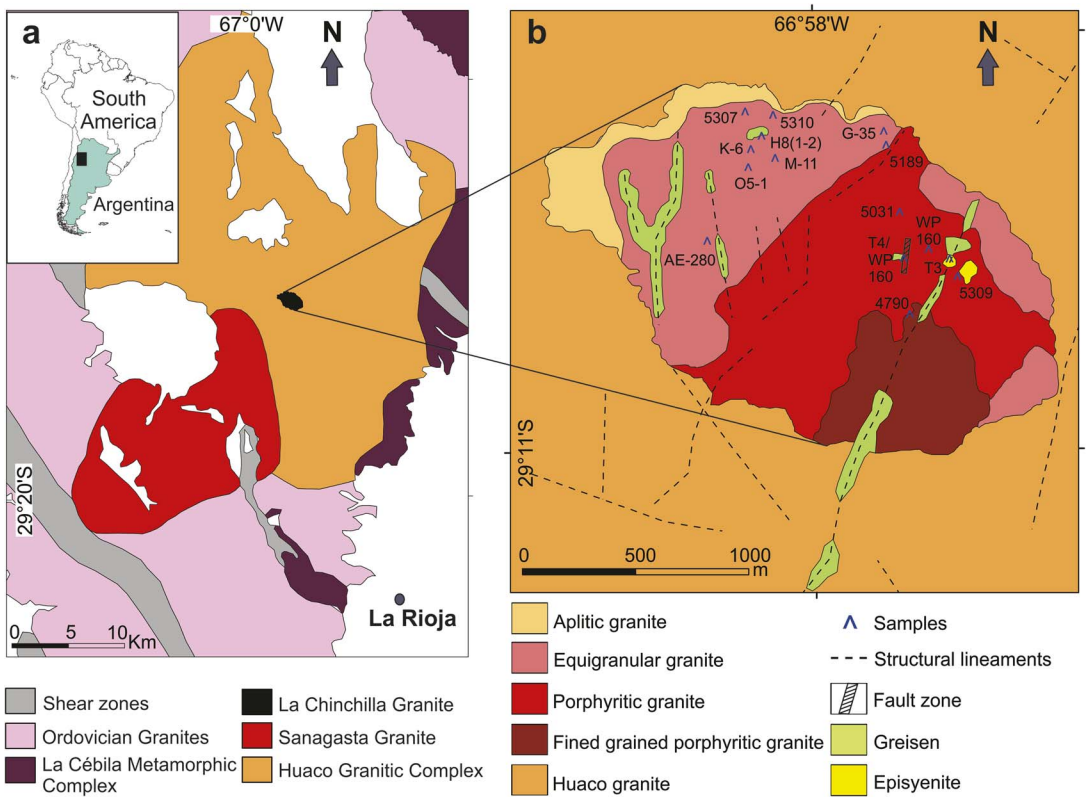

FIG. 1. (a) Location and geological setting of La Chinchilla pluton (modified from Grosse & Sardi 2005 and Grosse *et al.* 2009). (b) La Chinchilla granitic facies (modified from Salvatore *et al.* 2013) and main structurally controlled hydrothermal alteration lithologies (modified from Bardelli *et al.* 2018) with sampling spots studied in this work.

presence of xenotime and Nb-Ti-Th-bearing uranophane included in zircon in drill cores of the equigranular and porphyritic facies, as well as Nb-rich uranophane, galena, thorianite and Pb-Mn oxides, and other unidentified species. In faulted and altered granite areas Morello (2013a) and Morello & Aparicio González (2013) described a U-Nb-Ta secondary species that later was recognized as carlosbarbosaite (Morello 2013b); these authors also identified magnetite, hematite, anatase, and coronadite in the same altered areas. Other primary accessory species identified by Bardelli (2014) and Bardelli *et al.* (2018) in the porphyritic granite facies are columbite-(Fe), fergusonite-(Y), V-bearing cheralite, Nb-bearing ilmenite, tantite (or alumotantite?), gittinsite (or calciocatapleiite?), and a Ti-rich, Nb-Ta-Fe-Ca mineral of the betafite group.

Whole-rock chemistry typifies the La Chinchilla granites as metaluminous to weakly peraluminous (A/CNK range = <0.92–1.08, average 0.99), rich in SiO_2 (73.6–76.2 wt.%), alkalis (Na_2O = 3.4–4.2 wt.%; K_2O = 4.2–4.8 wt.%), and F (one sample of the porphyritic facies yielded 0.35 wt.% F). These granites are relatively poor in Fe_2O_3, MgO, CaO, Sr, and Ba and poor in P contents; a ferroan affinity shows up from its high Fe/Mg ratios (Grosse *et al.* 2009, Dahlquist *et al.* 2010, Bardelli *et al.* 2018). The elements Y, Nb, Ta, Th, U, REE, Li, Rb, and Be are notably enriched (Grosse *et al.* 2005, 2006). The U content is high; Grosse *et al.* (2009) registered values between 18 and 69 ppm, whereas Salvatore *et al.* (2013) obtained average U contents of 119 ppm for the equigranular facies and 28 ppm for the porphyritic facies in outcropping samples. Cuney (*pers. commun.*) reported an average of 27 ppm of U (14.4–36.7 ppm) in drill core samples of the porphyritic granite. The Nb contents of undifferentiated La Chinchilla granite practically double the Nb content of the enclosing Huaco granite facies (*i.e.*, average of 56.15 ppm Nb in four samples of the La Chinchilla granites *versus* 26.2 ppm Nb in five samples of the border and equigranular facies of the Huaco granite, ranging from 53.1 to 65.7 *versus* 22.6 to 32.9 ppm Nb, respectively).

Thermal modeling applied to field data (cross sections and mineral fabric measurements) allowed interpretation of the internal anatomy of the pluton as asymmetric, with a subhorizontal tabular to funnel-shaped geometry, being conceived as a small batch of magma that cooled down in less than 0.05 Myr, about 9 Myr after the enclosing Huaco granite (Macchioli Grande *et al.* 2019). Its emplacement could have been controlled by brittle fracturing and prevailing block displacement by stoping (Macchioli Grande *et al.* 2015, 2019). From a petrogenetic and geotectonic perspective, Dahlquist *et al*. (2010) proposed that prominent shear zones played a significant role in providing suitable conduits for the emplacement of A-type bodies like La Chinchilla and other neighboring units. This A-type plutonic episode in the region seems to be linked to an Andean-type margin (Alasino *et al.* 2012, Dahlquist *et al.* 2013).

The profuse occurrence of seriate-sized miarolitic pegmatites both in the porphyritic and equigranular granite facies (Lira *et al.* 2015) is indicative of the La Chinchilla body emplacement below ~2 kbar (*e.g.*, Candela 1997). In agreement, Alasino *et al*. (2010) estimated at 1.8 kbar the emplacement *P* of the nearby La Costa Carboniferous peraluminous pluton located ~50 km north of La Chinchilla and emplaced in a related geotectonic setting. The granitic facies and miarolitic pegmatites of the La Chinchilla pluton were overprinted by late, structurally controlled hydrothermal alteration processes, *i.e.*, episyenitization, silicification, and greisenization (Bardelli 2014, Bardelli *et al.* 2018).

La Chinchilla miarolitic pegmatites

The La Chinchilla equigranular facies is characterized by the presence of abundant, tiny miarolitic pegmatites that range in size from ~0.5 up to ~2 cm in diameter; this facies also hosts abundant larger bodies up to a couple of meters wide, showing a complete transition from centimeter- to meter-sized bodies. Miarolitic pegmatites are also common within the porphyritic facies, though less abundant and of more erratic distribution; most are identifiable under microscopic observation, though some isolated large ones up to ~2 m in diameter are also sporadically found (Lira *et al.* 2015, Bardelli *et al.* 2018). In both granitic facies, the millimeter- to few centimeter-sized pegmatitic units are almost completely lined up with suhbedral to euhedral crystals arranged into tight pegmatitic textures, normally with ill-defined or apparently absent zoning; the latter was better developed in tens of centimeter- to meter-sized bodies, which almost invariably have a cavity instead of a filled core.

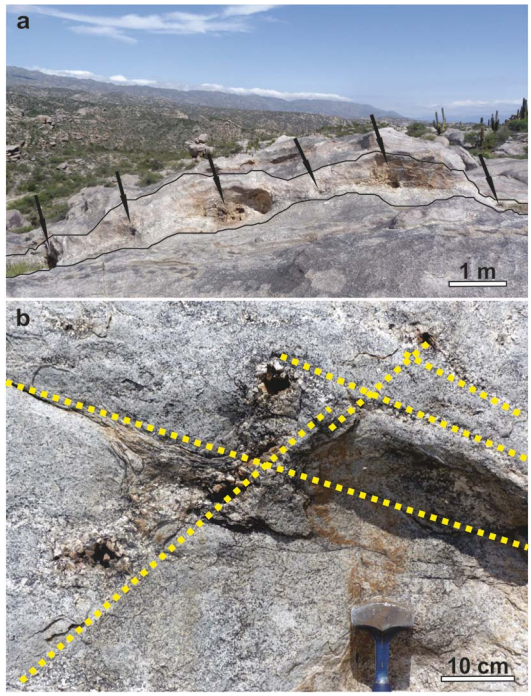

FIG. 2. (a) Interconnected miarolitic cavities (pinch-and-swell like structure) along a flow-like structural pattern of the pluton (N80°E–SSE dip; view to the SSE). (b) Other interconnected pegmatitic pods with miarolitic cavities, hosted in primary magmatic conjugate fractures during the ductile cooling stage; some of these types of melt-controlled emplacements show fracture cleavage evidence.

Some of the largest miarolitic pegmatites of the La Chinchilla pluton are typically interconnected along a pinch-and-swell structure, looking like rosary beads, aligned along a flow-like pattern of the pluton of dominant N80°E strike and SSE dip (Fig. 2a); others are also interconnected but following conjugate systems of an anastomosed fracturing network (*e.g.*, Janeczek 2007), likely primary magmatic cooling joints (Fig. 2b). Zonation patterns are not obvious in all miarolitic cavities; most of the transitions to the granite are diffuse, but others show millimeter- to a few centimeter-thick border and wall zones (*e.g.*, Fig. 3a). A clear distinction between these two zones was not always obvious, in agreement with the observations of Thomas & Davidson (2016), who noted that zone 1 (~2 mm-thick cryptocrystalline contact between granite and the beginning of pegmatite with an aplitic zone) and zone 2 (aplitic zone) may be absent in some bodies. In a few cases, 1 to 4 cm-long bladed, dark greenish mica crystals are disposed in stockade texture concentrated between the border and the roots of the

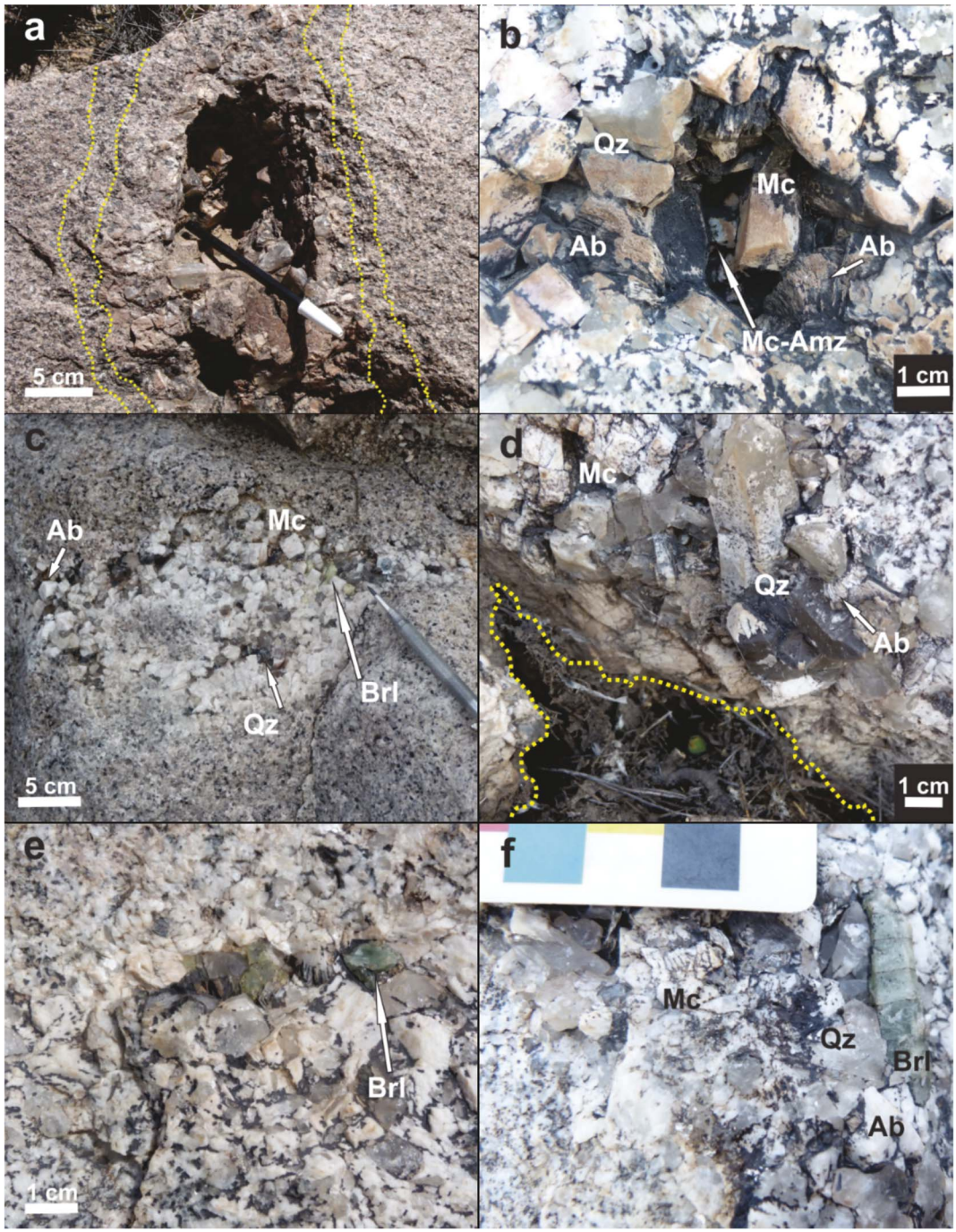

FIG. 3. (a to f) Common occurrences of miarolitic pegmatites and cavities hosted in the equigranular facies of La Chinchilla pluton. Abbreviations: Ab – albite (cleavelandite variety), Brl – beryl, Mc – microcline, Mc-Amz – amazonite variety, Qz – quartz (predominantly smoky). (b) Dark coatings are lichen. (f) Each rectangle of the scale represents 1 cm.

intermediate zone of radiating miarolitic crystals. Zone 3 (graphic granite) of Thomas & Davidson (2016) has been distinguished in a few outcrops but mostly under the microscope and is represented by ill-defined quartz-microcline graphic intergrowths of scarce development. Zone 4, coarsely crystalline feldspar and quartz with pegmatitic texture, is normally present. Zone 5 is the most common one found at La Chinchilla (Fig. 3a–f). It is characterized by cavity-lining crystals, majoritarily idiomorphic K-feldspar (sporadically the amazonite variety), albite (frequently the cleavelandite variety as fan-shaped lamellar aggregates, *e.g.*, Fig. 3b), and quartz (mostly gray or smoky, some up to 5 cm-long idiomorphic crystals). Booklets of light mica (muscovite) are less common. Prismatic beryl is a frequently found species that might occur as up to 5 cm-long crystals; no gemmy varieties were found and none of the several examined beryl crystals was found grown into void pockets (*e.g.*, Fig. 3c, e, f). Dark green beryl rarely occurs as tight aggregates of suhbedral crystals that form 2–3 cm-thick, <1 m-long lens-shaped veins within the equigranular facies. Zone 6 (the miarolitic cavity *s.s.*) might be empty in numerous of the largest miarolitic pegmatites or filled up with massive gray (or smoky) quartz (equivalent to the quartz core of Thomas & Davidson 2016) or light purple fluorite. All identified rare element (Nb, Ta, U, Th, Sn, Zr, Bi, and LREE) minerals were found in this zone, normally as inclusions in quartz or fluorite and albitized zones of amazonite.

Tabular subhorizontal aplitic bodies (N80°E, 10 to 50 cm thick) are also frequent in the La Chinchilla pluton; these dikes were emplaced along the ~E–W striking magmatic foliation described by Macchioli Grande *et al*. (2019). A particular outcrop showed symmetric pegmatitic wall zones ~5 cm thick, with typical bladed dark mica partially replaced by white mica in direct contact with a central zone of grayish aplite. Similar occurrences of pegmatite-aplite synmagmatic lenses or dike-like differentiates up to ~2 m thick were described by Parra & Bello (2009, CNEA unpublished report), 20 to 50 m below the collar, in several logged drill cores (*e.g.*, G-35, H8, K-6, M-11).

A post-crystallization widespread rupture process affected the largest pockets of miarolitic pegmatites, leaving most crystals (*i.e.*, K-feldspar, smoky quartz) either broken into pieces or fractured. Crystal fragments of dominating species were preserved *in situ* where the cavities were protected from erosion, but a large number of broken or chipped crystals are noticeably scattered on the topographic surface elsewhere over a large area. In addition to the most conspicuous broken crystals and shards of quartz and feldspars, other indicators might suggest fluid loss after rupture of the pockets (*e.g.*, Laurs *et al.* 1998, and references therein). These indicators are the radial lamellar overgrowths and replacements of albite (cleavelandite), feeble etching signals on mineral surfaces (*e.g.*, roughened or frosted crystal faces) and weak alteration (poor or absent fine-grained muscovitization or clay formation on feldspars). Some early crystals lining miarolitic cavities were healed by infilling/replacing smoky quartz in patches or veinlets, crosscut by microfractures with myriads of secondary fluid inclusions (*e.g.*, T4 exploration trench, Fig. 1b). In addition, in some pockets affected by late fault zones, as in the T4 exploration trench, smoky quartz shows well developed undulatory extinction and formation of grain subdomains as a result of postmiarolitic brittle tectonics.

Sampling and Analytical Methods

Field work allowed the recognition of granite facies zonation mapped by previous workers. Sampling was done across the different granite facies and miarolitic pegmatites, from outcrops (*i.e.*, samples 5309, 5310, WP195, WP160, 4790, 5031, 5189, and 5307), as well as from drill core at different depths (*i.e.*, samples H8-1, H8-2, AE-280, O5-1). Thin sections were routinely described under refracted and reflected plane polarized light.

Quantitative analyses of major and minor elements were obtained with a JEOL JXA 8230 electron probe micro-analyzer (EPMA) using wavelength dispersive spectrometry (WDS). The operating conditions were 15 kV accelerating voltage, 20 nA probe current (10 nA for feldspars), and counting times of 10 s for peak and 5 s for each background, using a probe diameter of 3–5 μm. The analyses were corrected for electron beam/matrix effects and instrumental drift and dead time using φ(ρZ) correction procedures (CITZAF; Armstrong 1995). The detection limits, standards and reference materials used for each element are as follows: F *K*α (0.045 wt.%, topaz), Na *K*α (0.008 wt.%, $NaNbO_3$/albite), Mg *K*α (0.005 wt.%, MgO/forsterite), Al *K*α (0.006 wt.%, albite/anortite), Si *K*α (0.012 wt.%, forsterite/anortoclase), P *K*α (0.015 wt.%, libethenite), Cl *K*α (0.003 wt.%, sodalite), K *K*α (0.025 wt.%, orthoclase), Ca *K*α (0.010 wt.%, $CaWO_4$/anorthite), Sc *K*α (0.021 wt.%, $ScVO_4$), Ti *K*α (0.022 wt.%, ilmenite), Cr *K*α (0.014 wt.%, chromite), Mn *K*α (0.024 wt.%, pyrolusite/rhodonite), Fe *K*α (0.025 wt.%, hematite/fayalite), Zn *K*α (0.022 wt.%, ZnO), As *L*α (0.029 wt.%, nickelin), Sr *K*α (0.018 wt.%, celestine), Y *K*α (0.016 wt.%, samarskite), Zr *K*α (0.014 wt.%, ZrO_2), Nb *L*α (0.029 wt.%, $NaNbO_3$), Sn *L*α (0.015 wt.%, cassiterite), Cs *L*α (0.024 wt.% pollucite), Ba *L*α (0.023 wt.%, baryte), La *L*α (0.022 wt.%, LaF_3), Ce *L*α (0.023 wt.%, $CeAl_2$/$CePO_4$), Nd *L*α (0.023 wt.%, NdF_3/$NdPO_4$), Ta *M*α (0.022 wt.%, simpsonite),

W $M\alpha$ (0.045 wt.%, $CaWO_4$), Pb $M\alpha$ (0.028 wt.%, galena/pyromorphite), Th $M\alpha$ (0.015 wt.%, ThO_2), and U $M\alpha$ (0.066 wt.%, U_3O_8). Some accessory mineral phases less than ~30 μm in size were identified by means of energy dispersive spectrometry (EDS) in the same EPMA system.

Results

Petrography of the two main granite facies: Equigranular and porphyritic

Equigranular granite. The equigranular facies shows a variable range of grain size (~250 μm to 7 mm), but the volumetrically dominant grain size ranges from 1.5 to 3 mm. K-feldspar shows identical textural features in both facies; it occurs as anhedral grains with cross-hatched twinning both in small grains and in late, moderately argillitized crystals up to 7 mm. Larger K-feldspar crystals are poorly perthitic and commonly poikilitic (tabular plagioclase, drop-like quartz, and muscovite inclusions). Symplectitic textures show up between mica and quartz reactive borders. K-feldspar is partially replaced by secondary albite. Two analyses of K-feldspar of the equigranular granite (sample 5310) are within the range $Or_{91.4-93.8}Ab_{8.6-6.2}$, whereas one analysis of the porphyritic granite yielded $Or_{96.4}Ab_{3.6}$. Plagioclase (albite) is normally tabular subhedral and of smaller grain size; it occurs in both facies as small crystals included in quartz and microcline or as larger tabular crystals often with quartz, fluorite, and zircon inclusions, and may be altered to clay minerals and muscovite. Anhedral quartz co-crystallized with microcline are the main components, followed by subordinate amounts of plagioclase, micas, fluorite, beryl, zircon, monazite-(Ce), fluorapatite, and other HFSE (high field strength element) oxide accessory phases already described by Bardelli *et al*. (2018), most of which are also present in the porphyritic granite (see below). The composition of plagioclase of the equigranular granite is within the following ranges (sample 5310): $Ab_{95.2-99.1}Or_{1.4-0.5}An_{3.4-0.4}$ (dataset in Supplementary Data 1)[1]; albite with ~95% mol Ab (sample 5310) is the least differentiated analyzed plagioclase. Colorless to spotty-colored purple fluorite (up to 2 mm) occurs in both facies but is the main accessory phase of the equigranular granite; it occurs as late anhedral grains, in some cases tending to euhedral shapes. Beryl is a relevant accessory phase present in both facies as small anhedral crystals. Zircon is common as inclusions in micas, plagioclase, microcline, and fluorite. Thorium-bearing monazite-(Ce) was found in euhedral and subhedral crystals either included in micas or mostly hosted by feldspars. Fluorapatite is scarce and occurs as inclusions in mica and quartz.

Porphyritic granite. The porphyritic facies was texturally divided into two subfacies: medium to coarse-grained (~4–6 mm) and fine- to medium-grained (~2–3 mm) groundmass. The first one shows millimeter- to microscopic-sized miarolitic cavities and bears K-feldspar phenocrysts (1 to 4 cm); the finer-grained matrix exhibits smaller phenocrysts (±2 cm). One K-feldspar analysis of the coarse-grained porphyritic facies (sample 5309) yielded $Or_{96.4}Ab_{3.6}$ (molar composition); the average of two plagioclase analyses of the same sample is $Ab_{98.1}Or_{0.69}An_{1.2}$. Plagioclase from the fine-grained porphyritic facies (sample 4790) varies within the ranges of $Ab_{97.3-99.4}Or_{0.4-0.9}An_{0.0-1.9}$ (dataset in Supplementary Data 1).

The coarse-grained subfacies is areally dominant; it is mainly formed of quartz, K-feldspar, plagioclase, and micas of the siderophyllite–protolithionite series. Albite, smoky quartz, and muscovite are present as late stage magmatic phases (Bardelli *et al.* 2018). A rich and varied accessory mineralogy commonly includes zircon, fluorite, beryl, less frequent fluorapatite, and minor amounts of several HFSE oxide species [*e.g.*, columbite-(Fe), cheralite, fergusonite-(Y), gittinsite (or calciocatapleiite?), pyrochlore supergroup species, tantite?, thorianite, and xenotime]. Anhedral to subhedral, polygranular, fine-grained ilmenite (up to 50 μm) is frequent as inclusions in micas.

The most conspicuous features at the transition zone to micropegmatitic domains in both granite types at a thin section scale are the increase of grain size, on occasion weakly perceptible, toward the empty cavity or more frequent filled core, and the sudden appearance of ill-defined pegmatitic textures, *e.g.*, graphic/granophyric and symplectitic intergrowths, bladed dark micas, and the idiomorphism of microcline and albite (Ab 1) grown into voids or late infilling quartz (Fig. 4a–d). Intergranular, centripetal albitization of earlier plagioclase and microcline becomes more intense in proximity to miarolitic assemblages, developing fine-grained albite (Ab 2) in chessboard aggregates (*e.g.*, Fig. 4d). Some miarolitic domains show kaolinization after feldspars, more intense over sectors of strong albitization and fluorite deposition.

Mineralogy and mineral chemistry of miarolitic species

K-feldspar (amazonite). Amazonite idiomorphic crystals were found in a few clustered miarolitic cavities scattered over an area of about 500 m^2 (*e.g.*, sample 5307; Fig. 1). These occur associated with smoky

[1] Supplementary Data are available from the Depository of Unpublished Data on the MAC website (http://mineralogicalassociation.ca/), document "Carlosbarbosaite from the La Chinchilla Pluton, CM61, 23-00008".

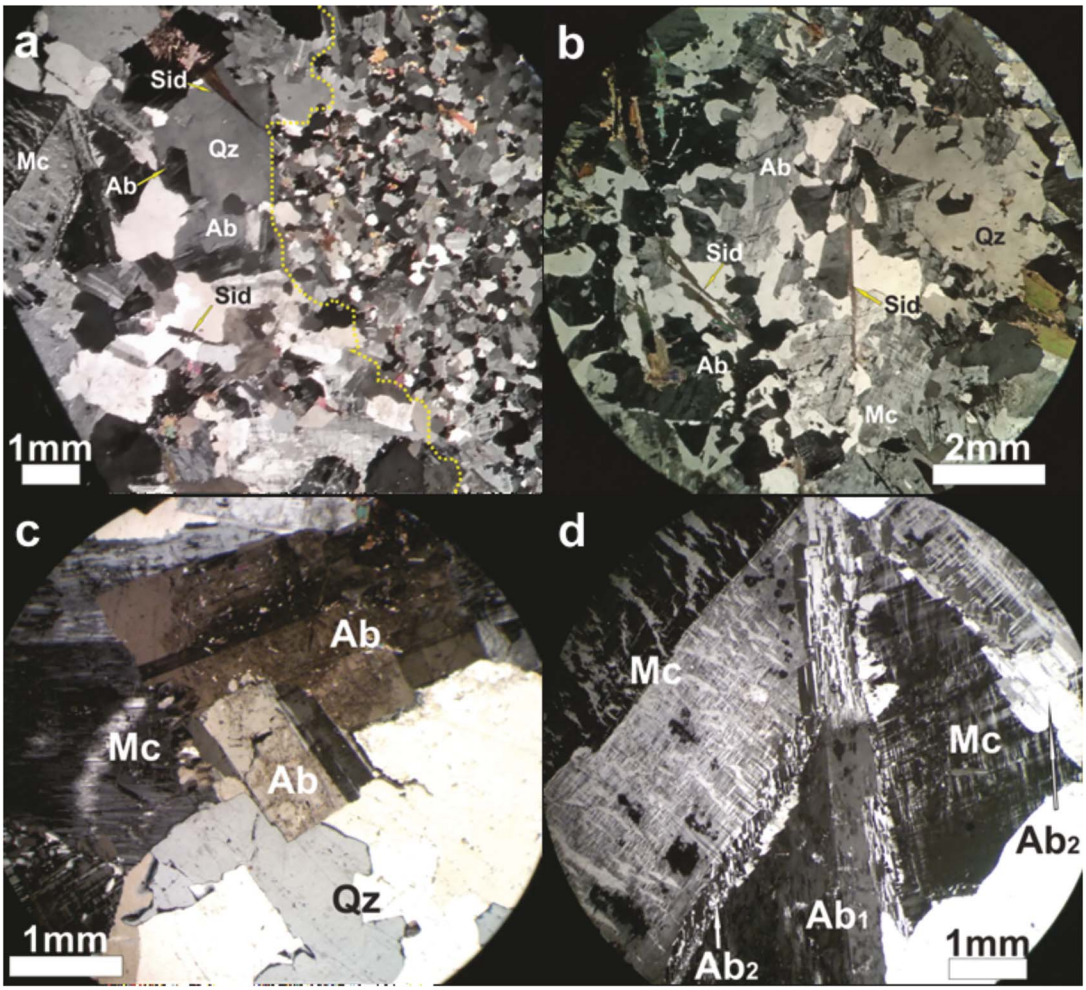

FIG. 4. Common textural changes that characterize the boundary zone between granite and micropegmatitic/miarolitic domains. (a) Abrupt grain size variation at the boundary; bladed siderophyllite (Sid), Carlsbad-twinned cross-hatched perthitic microcline (Mc), and euhedral albite (Ab 1) with sharp wedged polysynthetic twinning and large anhedral late quartz (Qz) are typical in the coarse-grained micropegmatite/miarolitic domain. (b) Graphic/granophyric intergrowths, bladed siderophyllite, and larger quartz patches. (c) Albite (Ab 1) with idiomorphic contours preceded quartz infill. (d) Carlsbad-twinned perthitic microcline crystals and Ab 1 with albitized intercrystalline contacts; fine-grained albite (Ab 2) crystals developed chessboard textures.

quartz and albite (± beryl), showing the dominant crystal forms (110), (010), and (011) (*e.g.*, Fig. 3b); the crystal fragments range in size from ~3 up to ~6 cm long. Intergrown Carlsbad-twinned individuals are common. Amazonite is pale blue to greenish with an outer ~5 mm-thick noticeable whitish rim (Fig. 5); growth of the rim on preferential crystal faces could not be determined. Amazonite crystals from representative samples 5307 (a-b-c) were examined in thin section and through X-ray diffraction (XRD) and WDS. Microcline is veinpatchy perthitic (~20–25% vol. of exsolved Ab). No differences other than color zonation are microscopically evident, with optical continuity between the colored core and the whitish rim. The distribution and intensity of coloration is quite irregular, as is the Pb content.

Amazonitic microcline hosts two generations of albite: (1) lamellar albite 1 crystals (~1 mm long) are regularly distributed, looking like inclusions from the inner to the outermost crystal zones; (2) finer-grained albite 2, locally with chessboard texture, selectively

FIG. 5. Polished slab of crystal fragment of rimmed amazonite from meter-sized, ruptured miarolitic cavity. Ruler scale in centimeters. Fe-oxide/hydroxide stains along cracks.

replaces the perthite fraction. In one crystal fragment, replacement albite 2, in association with extremely F-rich polylithionite and fluorite, hosts cassiterite, hydroxycalciopyrochlore, and late monazite-(Ce).

In terms of molar endmembers, the composition of microcline in both the inner colored zones and the outer pale rims is practically identical, within the ranges of $Or_{92.3-95.8}Ab_{7.7-4.2}$ (dataset in Supplementary Data 2). Perthitic albite is slightly enriched in K ($Ab_{99.5}Or_{0.5}$) when compared with the average composition of lamellar albite ($Ab_{99.0}Or_{0.93}An_{0.07}$). Trace concentrations of Pb, Cs, and P were analyzed by EPMA (dataset in Supplementary Data 2). Except for Pb, the contents of Cs and P were below detection limits. Lead was detected in both the inner and outer zones of the crystals. The range of PbO in the core varies from low contents above detection limits (a.d.l., *i.e.*, 300 ppm PbO) up to 680 ppm, and in the rim from a.d.l. up to 470 ppm. Distribution of Pb seems to be irregular with marked Pb content variation in distances <1 mm, more noticeable in the rim where Pb is undetectable in larger areas. PbO averages of both zones are in the range of 330 (core) to 430 (rim) ppm. A positive correlation between the concentration of Pb and the intensity of coloration could not be established.

Powder XRD analyses performed in both the colored inner part of a crystal and the outer whitish rim correspond to maximum low microcline (triclinicity indexes calculated after Goldsmith & Laves 1954 and McGregor & Ferguson 1989). The *c* and *b* cell parameters in the colored core zone have slightly lower dimensions, trending to a less ordered intermediate member, thus with a reduction of the cell volume from the outer rim to core (720.8 to 719.3 $Å^3$, respectively; Lira *et al.* 2015).

Beryl. At the La Chinchilla pluton, beryl occurs in both the equigranular and porphyritic granites. It is more abundant in the equigranular granite where it may exhibit the following modes of occurrence: (1) as the main granitic accessory phase (<1%) in disseminated, pale green, anhedral to subhedral crystals (0.3 to 2 mm), normally associated with fluorite in the micropegmatitic domains; (2) as idiomorphic short prismatic crystals in miarolitic pockets and pegmatites where it shows bluish green to deep green color and may reach up to 2 cm long (Fig. 3c, e, f), commonly associated with microcline, albite (cleavelandite), colorless fluorite, muscovite, and well developed smoky quartz crystals; and (3) occasionally as dark green veinlets (up to 1 cm thick) that crosscut the equigranular granite at the northern pluton boundary (PF-21 CNEA core samples).

In the porphyritic granite, beryl occurs mainly as small anhedral accessory grains, also spatially restricted to the micropegmatitic domains. An abnormally high concentration of fine- to medium-grained light green beryl crystals occur in a silicification halo that externally bounds an episyenitic alteration lens within a micropegmatitic zone in the porphyritic granite, associated with fluorite and probable bismuth carbonates.

Major element chemistry data for beryl from a few analyses from La Chinchilla do not differ significantly from data from more detailed studies of Sardi *et al.* (2013, 2016). Average values of beryl analyses from the La Chinchilla equigranular granite facies (Sardi *et al.* 2016) are as follows (in wt.%): 62.8 SiO_2, 17.3 Al_2O_3, 12.8–13.1 BeO (calculated), 0.8 FeO_t, 0.03 MnO, 0.02 MgO, 0.02 CaO, 0.13 Na_2O, and 0.01 K_2O. The sum of divalent cations is very low, Fe being the main one of the octahedral site (FeOt ≫ MgO+MnO); the Na content is also low but dominant over K, thus it was classified as sodic beryl; cationic substitutions were minor (Sardi *et al.* 2016). The weight percentages of MgO, Na_2O, and K_2O are equivalent to those of beryl from the Velasco District pegmatites, considered to be of a mid to low degree of evolution (Sardi & Heinman 2014, Sardi *et al.* 2016).

Pale green miarolitic beryl WDS analyses from samples 5310 (equigranular facies) and 5309 (porphyritic facies) are tabulated in Supplementary Data 3. The average of three analyses of sample 5310 yielded (in wt.%) SiO_2 65.28, TiO_2 0.04, Al_2O_3 16.72, FeOt 2.74, BeO (calculated) 13.30, MnO 0.06, MgO 0.04, Na_2O 0.29, K_2O 0.04, and Cs_2O b.d.l.; the average formula of three analyses is $(Na_{0.05}K_{0.01})_{\Sigma 0.06}(Be_{2.95}Li_{0.05})_{\Sigma 3}(Al_{1.82}Fe_{0.20}Mn_{0.01}Mg_{0.01})_{\Sigma 2.04}Si_{6.03}O_{18}$. The composition of sample 5309 is (in wt.%) SiO_2 65.43, TiO_2 0.06, Al_2O_3 18.17, FeOt 1.00, BeO* 13.56, MnO 0.00, MgO 0.01, Na_2O 0.30, K_2O 0.04, Cs_2O 0.10. The formula of beryl from the porphyritic granite (5309) is

TABLE 1. REPRESENTATIVE ANALYSES OF POLYLITHIONITE (OXIDE DATA IN wt.%) FROM LA CHINCHILLA GRANITES AND MIAROLITIC PEGMATITES

Sample	5307b-2	5307b-3	5307b-4	5307b-7	5307b-8	5307b-9	5307b-10
SiO_2	53.84	52.50	52.73	52.30	53.10	54.16	50.12
TiO_2	0.12	0.04	0.08	0.06	0.08	0.07	0.00
Al_2O_3	17.56	17.48	17.64	18.11	17.81	17.47	18.70
ZnO	0.07	0.07	0.06	0.11	0.02	0.04	0.04
FeO	5.76	5.87	5.63	6.50	6.53	5.77	7.42
MnO	1.71	1.39	1.46	1.79	1.61	1.45	1.92
MgO	0.08	0.05	0.07	0.08	0.09	0.09	0.08
CaO	0.01	0.02	0.02	0.01	0.01	0.02	0.02
BaO	0.09	0.16	0.00	0.05	0.05	0.02	0.07
Na_2O	0.06	0.08	0.09	0.06	0.08	0.10	0.04
K_2O	10.63	10.59	10.42	10.83	10.97	10.79	10.43
F	9.90	9.22	9.32	10.01	10.01	10.03	8.94
Cl	0.00	0.00	0.02	0.01	0.00	0.00	0.00
Li_2O*	5.90	5.51	5.58	5.46	5.69	5.99	4.83
H_2O**	0.00	0.00	0.00	0.00	0.00	0.00	0.00
Sum	105.74	103.00	103.13	105.37	106.06	106.00	102.60
O=F.Cl	4.17	3.88	3.93	4.22	4.22	4.22	3.76
Total	101.57	99.11	99.20	101.16	101.84	101.78	98.84
Si	7.219	7.210	7.212	7.110	7.152	7.240	6.991
Al(IV)	0.781	0.790	0.788	0.890	0.848	0.760	1.009
ΣT	8.000	8.000	8.000	8.000	8.000	8.000	8.000
Al(VI)	1.993	2.040	2.056	2.012	1.980	1.992	2.065
Ti	0.012	0.004	0.009	0.006	0.008	0.007	0.000
Zn	0.007	0.007	0.006	0.011	0.002	0.004	0.004
Fe	0.646	0.674	0.644	0.739	0.736	0.645	0.866
Mn	0.194	0.162	0.169	0.206	0.184	0.164	0.227
Mg	0.016	0.011	0.015	0.017	0.018	0.017	0.016
Li	3.182	3.046	3.070	2.983	3.081	3.222	2.708
ΣM	6.051	5.943	5.968	5.974	6.009	6.052	5.885
Ca	0.001	0.004	0.003	0.001	0.002	0.002	0.003
Ba	0.005	0.009	0.000	0.002	0.002	0.001	0.004
Na	0.015	0.022	0.023	0.017	0.022	0.026	0.012
K	1.818	1.855	1.818	1.878	1.885	1.840	1.856
ΣA	1.839	1.890	1.845	1.899	1.911	1.869	1.875

* Li_2O was calculated with the equation [$Li_2O = (0.289 * SiO_2) - 9.658$ (Tischendorf *et al.* 2004) for micas with MgO < 3 wt.%, Al_2O_3 < 26 wt.%, and F > 4 wt.%.
** H_2O content calculated on the basis of charge balance.
Total iron expressed as Fe^{2+}.

$(Na_{0.05})_{\Sigma 0.05}(Be_{2.98}Li_{0.02})_{\Sigma 3}(Al_{1.96}Fe_{0.08})_{\Sigma 2.04}Si_{5.98}O_{18}$. The main differences in the chemical compositions of both beryl samples consist of the much higher occupancy of Al in the octahedral site (almost free of substituting divalent cations, Fe ~ 8%) and up to 1000 ppm of Cs_2O in sample 5309 *versus* ~22% octahedral site occupancy (Fe > Mn = Mg) and undetectable Cs in beryl from sample 5310.

Polylithionite. The chemical composition of hydrothermal late-miarolitic micas is displayed in Table 1. Micas of sample 5307b are extremely rich in F (average 9.63 wt.% F, range between 8.94 and 10.03 wt.% F, $n = 7$). These micas have a high SiO_2 content (average SiO_2 = 52.68 wt.%, range 50.12 to 54.16), with an Al_2O_3 average content of 17.82 wt.% (range from 17.47 to 18.70 wt.%). In the scheme proposed by Tischendorf *et al.* (2007), these extreme F-rich micas are classified as polylithionite (average Li_2O = 5.56 wt.%).

Pyrochlore supergroup minerals. Species of the pyrochlore supergroup occur in two types of paragenetic associations: Pyrochlore type 1: A species described by Lira *et al.* (2015) as an "unidentified

opaque phase of the composition Si-Nb-Ca-Ti-Fe" was identified as a member of the pyrochlore supergroup. It occurs as 1.5 to 2 mm needle-like granular aggregates, intergrown with ~100 μm-sized cassiterite grains in its periphery (sample 5307, Fig. 6a). Both species are included in metasomatic-hydrothermal albite that replaces amazonitic microcline associated with extremely F-rich polylithionite and fluorite (analyses 5307B, points 10 to 14, Table 2). Pyrochlore type 2: Sample 5307 also bears pyrochlore grains but with a distinct mode of occurrence and mineral association; it occurs in a granular aggregate up to 650 μm as an incomplete replacement of Th-bearing monazite-(Ce) associated with purple fluorite. Type 2 pyrochlore grains are cracked and notoriously metamictic, showing bad polishing, negative relief, and variable low analytical totals (~93–96 wt.%; analyses 5037b, points Pyr4-8-9-10-11, Table 2; Fig. 6b).

EPMA analyses (Table 2; $n = 11$) were done on pyrochlore types 1 and 2. These were normalized to six oxygen atoms and two *apfu* in the *B* site based on the classification proposal of Atencio *et al*. (2010) and further considerations (Atencio 2013, Christy & Atencio 2013, Atencio 2021). In this scheme, the sum of cation valences < 13.5 and with OH dominant in the *Y* site ($F < 0.5$ *apfu*, 0.19 wt.%), most of the analyzed crystals correspond to hydroxycalciopyrochlore, with one analysis within the hydroxycalciomicrolite field. Hydroxycalciopyrochlores and hydroxycalciomicrolites from the La Chinchilla miarolitic pegmatites are SiO_2-rich (average content = 9.47 wt.%, 0.550 *apfu*). Significant chemical differences exist between pyrochlore type 1 (associated with cassiterite 2), replacing an unknown species, and type 2, partially replacing monazite-(Ce). Type 2 pyrochlore is notoriously richer in SiO_2, P_2O_5, UO_2, and PbO and poorer in FeO and TiO_2 than type 1 (in wt.%): SiO_2 10.22 *versus* 8.73, P_2O_5 4.71 *versus* 3.24, UO_2 4.62 *versus* 2.62, PbO 4.38 *versus* 2.30, FeO 1.43 *versus* 6.27, and TiO_2 1.64 *versus* 3.51. Despite the fact that pyrochlore type 2 replaces Th-bearing monazite-(Ce), its ThO_2 content is identical (within the range of analytical uncertainty) to that of pyrochlore type 1. The Ta# [Ta/(Nb+Ta)] is also higher in type 2 hydroxycalciopyrochlore which evolves into hydroxycalciomicrolite (type 1 = 0.381, type 2 = 0.478). Pyrochlore supergroup species were plotted in the Nb–Ti–Ta ternary diagram (Fig. 7a) used by Hogarth (1977) with new delimited fields proposed by Atencio *et al*. (2010) and the discriminatory compositional fields of Mackay & Simandl (2015). The same data were plotted in the ternary diagram of De Ignacio *et al*. (2012), the discriminatory fields of which were drawn with data of Williams *et al*. (1997) and Nasraoui & Bilal (2000) based on *A*-site cations and vacancies (Fig. 7b).

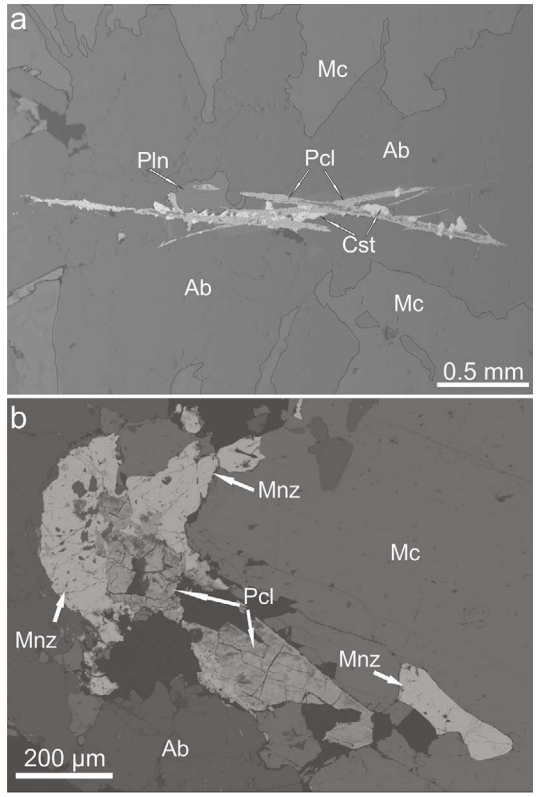

FIG. 6. (a) Backscattered electron image (BSE) of type 1 hydroxycalciopyrochlore (Pcl) and cassiterite 2 (Cst) replacing unknown needle shaped crossed crystals included in cleavelandite (Ab) that replaces amazonite (Mc), associated with F-rich polylithionite (Pln) and fluorite (not shown in the image). (b) BSE image of type 2 hydroxycalciopyrochlore–hydroxycalciomicrolite replacing Th-bearing monazite-(Ce) (Mnz); see text for alternative interpretations.

Hydroxycalciopyrochlores and hydroxycalciomicrolite from La Chinchilla are SiO_2-rich (average content ~ 9.5 wt.%), as high as some of the values for pyrochlores from Narssârssuk, Greenland (Bonazzi *et al*. 2006), and from the A-type peralkaline granites of the Katugin rare metal deposit, Transbaikalia, Russia (Starikova *et al.* 2019). Higher SiO_2 values (up to ~13 wt.%) were found by Dumanska-Slowik (2014) in fluornatropyrochlores of the nepheline syenites of the Mariupol Massif, SE Ukraine. Despite current uncertainties regarding how much Si could be allocated in the *B* site of crystalline pyrochlore and to what extent it could be incorporated by contamination into eventual localized radiation damaged sectors (*i.e.*, Bonazzi *et al.* 2006, Atencio *et al.* 2010, Dumanska-Slowik 2014, Deditius *et al.* 2015), we adopted the suggestion of Bonazzi *et al*. (2006) to assign

TABLE 2. ELECTRON MICROPROBE ANALYTICAL RESULTS (IN OXIDE wt.%) AND CALCULATED MINERAL FORMULAE OF PYROCHLORE GROUP MINERALS FROM LA CHINCHILLA MIAROLITIC AND MICROPEGMATITIC ASSEMBLAGES

Sample	5307B-10	5307B-11	5307B-12	5307B-13	5307B-14	5307B-Pyr 4	5307B-Pyr 8	5307B-Pyr 9	5307B-Pyr 10	5307B-Pyr 11
Na_2O	0.59	0.20	0.46	0.40	0.43	0.48	0.74	0.61	0.69	0.44
CaO	6.71	7.58	7.39	7.96	7.99	7.51	7.31	7.17	7.16	8.32
MnO	0.61	0.55	0.49	0.61	0.49	0.12	0.12	0.14	0.20	0.13
SrO	0.36	0.44	0.49	0.60	0.50	0.54	0.61	0.53	0.45	0.48
BaO	0.38	0.23	0.28	0.35	0.38	0.30	0.26	0.30	0.26	0.37
FeO	8.92	5.50	4.74	5.83	6.34	1.42	1.59	1.42	1.49	1.21
PbO	2.03	2.41	2.56	2.00	2.48	4.62	4.57	4.37	4.22	4.13
Y_2O_3	0.22	0.32	0.15	0.35	0.24	0.01	0.09	0.01	b.d.	0.30
Ce_2O_3	2.04	1.96	1.63	1.73	1.60	0.60	0.94	0.78	1.25	1.34
La_2O_3	0.10	0.31	0.15	0.27	0.14	0.21	0.16	0.24	0.25	0.24
Nd_2O_3	0.03	0.10	0.05	b.d.	0.12	0.01	0.15	0.08	0.16	0.27
Sc_2O_3	0.19	0.18	0.10	0.16	0.08	0.10	0.11	0.10	0.11	0.11
UO_2	1.85	2.76	2.73	2.80	2.97	4.83	4.59	4.78	4.83	4.07
ThO_2	0.61	0.89	0.75	0.85	0.75	0.86	1.05	0.57	0.68	0.83
Ta_2O_5	25.30	29.33	31.01	28.61	25.80	29.60	29.37	32.11	28.23	32.84
Nb_2O_5	28.09	24.43	22.79	23.95	24.61	19.14	19.10	17.65	19.06	15.49
TiO_2	4.39	3.32	3.07	3.29	3.49	1.68	1.78	1.70	1.69	1.37
WO_6	1.16	1.22	1.49	1.49	0.87	0.80	0.88	0.92	0.87	0.79
As_2O_5	0.13	0.03	0.03	0.11	0.15	0.15	0.06	0.04	0.14	0.11
P_2O_5	2.63	3.30	3.44	3.54	3.27	4.87	4.79	4.53	4.84	4.54
SnO_2	0.35	0.41	0.16	0.14	0.14	0.48	0.44	0.35	0.35	0.38
ZrO_2	0.70	0.60	0.61	0.74	0.77	0.57	0.63	0.54	0.54	0.57
MgO	0.25	0.27	0.23	0.25	0.24	0.28	0.25	0.23	0.22	0.20
Al_2O_3	1.17	1.24	1.23	1.24	1.16	1.60	1.71	1.40	1.48	1.96
SiO_2	7.12	9.44	9.78	8.60	8.71	10.31	10.56	10.26	9.41	10.54
F	0.14	0.20	0.25	0.18	0.13	0.25	0.29	0.04	0.13	0.32
K_2O	0.43	0.17	0.37	0.29	0.30	0.30	0.53	0.27	0.65	0.28
Cs_2O	b.d.	b.d.	0.04	b.d.	0.08	b.d.	b.d.	b.d.	b.d.	b.d.
Total	96.51	97.38	96.45	96.31	94.23	91.64	92.68	91.14	89.36	91.63
O=F	0.06	0.08	0.10	0.08	0.05	0.11	0.12	0.02	0.05	0.13
H_2O*	2.96	3.12	3.12	2.99	2.88	3.11	3.09	3.02	2.95	2.93
Total**	99.41	100.42	99.47	99.22	97.07	94.64	95.65	94.14	92.25	94.42
				Structural formula based on $\Sigma B = 2$						
Na	0.074	0.024	0.058	0.051	0.056	0.063	0.097	0.082	0.094	0.060
Ca	0.470	0.525	0.518	0.562	0.577	0.545	0.528	0.534	0.540	0.625
Mn	0.034	0.030	0.027	0.034	0.028	0.007	0.007	0.008	0.012	0.008
Sr	0.014	0.016	0.019	0.023	0.020	0.021	0.024	0.021	0.018	0.020
Ba	0.010	0.006	0.007	0.009	0.010	0.008	0.007	0.008	0.007	0.010
Fe^{+2}	0.488	0.297	0.259	0.322	0.357	0.080	0.090	0.083	0.088	0.071
Pb	0.036	0.042	0.045	0.036	0.045	0.084	0.083	0.082	0.080	0.078
Y	0.008	0.011	0.005	0.012	0.009	0.000	0.003	0.000	0.000	0.011
Ce	0.049	0.046	0.039	0.042	0.040	0.015	0.023	0.020	0.032	0.034
La	0.002	0.007	0.004	0.007	0.003	0.005	0.004	0.006	0.006	0.006
Nd	0.001	0.002	0.001	0.000	0.003	0.000	0.004	0.002	0.004	0.007
Sc	0.011	0.010	0.005	0.009	0.005	0.006	0.006	0.006	0.007	0.007
U	0.027	0.040	0.040	0.041	0.045	0.073	0.069	0.074	0.076	0.064
Th	0.009	0.013	0.011	0.013	0.012	0.013	0.016	0.009	0.011	0.013
ΣA	1.231	1.072	1.037	1.160	1.209	0.921	0.961	0.936	0.976	1.013
m***	0.769	0.928	0.963	0.840	0.791	1.079	1.039	1.064	1.024	0.987

TABLE 2. CONTINUED.

Sample	5307B-10	5307B-11	5307B-12	5307B-13	5307B-14	5307B-Pyr 4	5307B-Pyr 8	5307B-Pyr 9	5307B-Pyr 10	5307B-Pyr 11
Ta	0.406	0.466	0.498	0.464	0.427	0.493	0.487	0.549	0.489	0.566
Nb	0.830	0.714	0.674	0.714	0.750	0.586	0.582	0.555	0.607	0.491
Ti	0.216	0.162	0.151	0.163	0.177	0.086	0.090	0.089	0.090	0.072
W	0.020	0.020	0.025	0.026	0.015	0.014	0.015	0.017	0.016	0.014
As	0.005	0.001	0.001	0.004	0.005	0.005	0.002	0.001	0.005	0.004
P	0.145	0.180	0.190	0.198	0.187	0.279	0.273	0.267	0.289	0.270
Sn	0.009	0.011	0.004	0.004	0.004	0.013	0.012	0.010	0.010	0.011
Zr	0.022	0.019	0.020	0.024	0.025	0.019	0.021	0.018	0.019	0.019
Mg	0.025	0.026	0.023	0.024	0.024	0.028	0.025	0.024	0.023	0.021
Al	0.090	0.094	0.095	0.096	0.092	0.128	0.136	0.115	0.123	0.162
Si*	0.233	0.305	0.320	0.284	0.293	0.349	0.356	0.357	0.331	0.370
Σ*B*	2.000	2.000	2.000	2.000	2.000	2.000	2.000	2.000	2.000	2.000
F	0.030	0.041	0.051	0.037	0.027	0.054	0.062	0.009	0.029	0.071
Cs	0.000	0.000	0.001	0.000	0.002	0.000	0.000	0.000	0.000	0.000
K	0.036	0.014	0.031	0.025	0.026	0.026	0.046	0.024	0.058	0.025
Σ*Y*	0.066	0.055	0.083	0.062	0.055	0.079	0.107	0.033	0.087	0.096
*n****	0.934	0.945	0.917	0.938	0.945	0.921	0.893	0.967	0.913	0.904
Ta/(Ta+Nb)	0.329	0.395	0.425	0.394	0.363	0.457	0.455	0.497	0.446	0.536

Analyses # 10,11,12,13 and 14 correspond to hydroxycalciopyrochlore type 1, and analyses Pyr 4 and Pyr 8 to Pyr 11 correspond to hydroxycalciopyrochlore to hydroxycalciomicrolite type 2. b.d.: below detection limit.

* H_2O content calculated on the basis of occupancy in *A* and *Y* sites as described by Atencio *et al.* (2010).

** Bi, Sb, V, Hf, and Rb: analyzed but not detected.

*** *m* and *n*: vacancies in *A* and *Y* sites, respectively. Si*: calculated assuming 50% of total wt.% SiO_2 in the *B* site.

up to 50% of total SiO_2 to the *B* site. Good Nb and Ti *versus* Si negative correlation trends of high r^2 (>0.85), particularly in type 1 pyrochlores, support partial allocation of Si in the *B* site, though bivariate correlation is weak or absent in type 2 pyrochlore. Considering that the La Chinchilla pyrochlores do exhibit metamictization effects, we assume that the remaining Si^{4+} could be stored in radiation damaged altered domains. Si-rich pyrochlore group minerals (so-called "silicified pyrochlores") are commonly found in geochemically evolved parageneses (Bonazzi *et al.* 2006), a fact also proved to be true for the Si-rich pyrochlores from La Chinchilla, which are genetically associated with a late F-rich albitization stage of miarolitic amazonite.

In the Nb–Ti–Ta ternary diagram (Fig. 7a), the La Chinchilla hydroxycalciopyrochlores fall in a free area of the lithological discriminant fields of Mackay & Simandl (2015). We suggest that this area is appropriate for late stage fluids fractionated from NYF pegmatites and parental A-type metaluminous to weakly peraluminous granites; even some mixed pegmatites (NYF ≫ LCT signature) could help to outline this new field. In Figure 7a the increasing Ta# with slightly decreasing Ti delineates two distinguishable evolving trends, one corresponding to hydrocalciopyrochlore type 1 and the other hydroxycalciopyrochlore type 2 that gradually enters the microlite field (hydroxycalciomicrolite), toward the peraluminous granite field.

The same data were plotted in the ternary diagram of De Ignacio *et al*. (2012, Fig. 7b). This diagram supports a replacement origin *via* hydrothermal-metasomatic processes for hydroxycalciopyrochlore/hydroxycalciomicrolite (types 1 and 2) associated with late albitization and fluorite deposition.

Cassiterite. Cassiterite was found in two samples, in isolated grouped crystals in micromiarolitic cavities of sample O5-1 (cassiterite 1, Fig. 8) and intimately associated with hydroxycalciopyrochlore type 1 in albitized amazonite of miarolitic pegmatite 5307 (cassiterite 2, Fig. 6a), both within the equigranular facies.

Cassiterite 1 of the O5-1 sample occurs as polygranular associations of subhedral crystals 0.15 to 0.5 mm long included in large subhedral albite crystals and late quartz of the micropegmatitic stage. WDS analyses (Table 3) yielded the following composition ranges in wt.%: SnO_2 90 to 96.2, CaO 1.14 to 1.29, Ta_2O_5 and Nb_2O_5 0.2 to 1.4 and 0.8 to 3.28, respectively, FeOt 0.6 to 1.54, and TiO_2 0.27 to 0.45; other elements listed in Table 3 are either undetectable or present in negligible and arguable amounts. The Ta# [Ta/(Ta+Nb)] ratio of O5-1 cassiterite varies from 0.1 to 0.21.

Cassiterite 2 grains of sample 5307 are subidiomorphic to idiomorphic crystals that range in size from 15 to

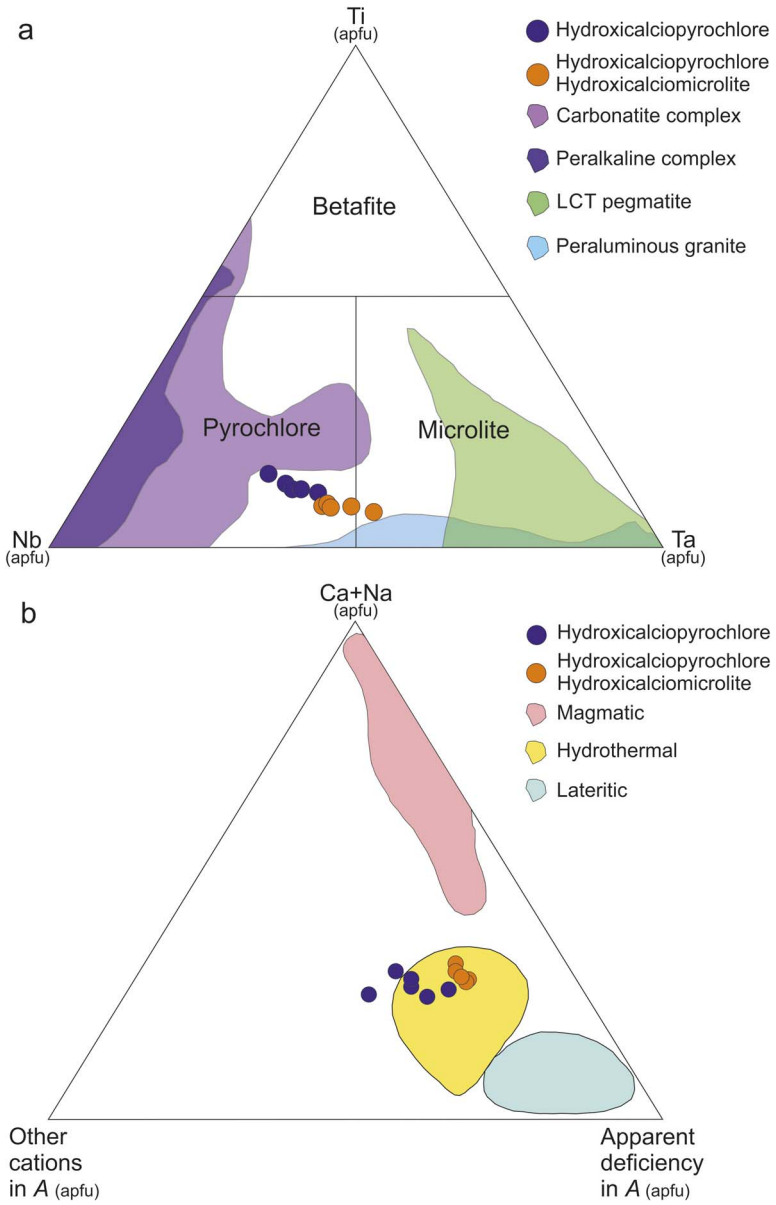

FIG. 7. (a) The Hogarth (1977) classification scheme of pyrochlore supergroup minerals modified by Atencio *et al*. (2010) with discriminatory petrogenetic fields according to Mackay & Simandl (2015). Hydroxycalciopyrochlore (type 1) replacing unknown fibrous species associated with cassiterite 2; hydroxycalciopyrochlore–hydroxycalciomicrolite (type 2) replacing monazite-(Ce). (b) Ternary diagram of De Ignacio *et al*. (2012) based on *A*-site cations and vacancies, with discriminatory fields for pyrochlore species formed from magmatic to supergene conditions (data of Williams *et al.* 1997 and Nasraoui & Bilal 2000). The plot supports the hydrothermal origin of hydroxycalciopyrochlore–hydroxycalciomicrolite from La Chinchilla.

100 μm; these crystallized immediately after hydroxycalciopyrochlore, where both formed as a pseudomorphic replacement of an unidentified fibrous to needle-like species included in albite crystal aggregates that replace amazonite. Of the two texturally distinct albite generations described above after amazonite replacement, cassiterite 2 is found associated with fine-grained albite 2, locally with chessboard texture, that selectively replaces

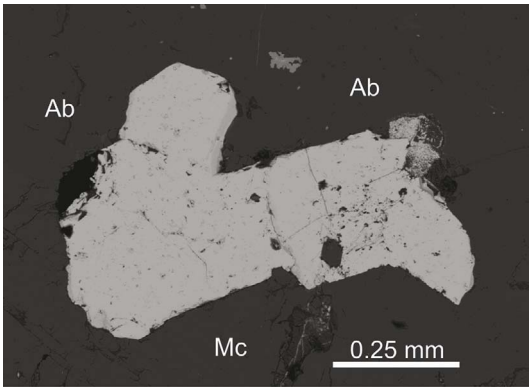

FIG. 8. Secondary electron image of cassiterite 1 crystal aggregates included in albite (Ab) and microcline (Mc) from a micropegmatitic domain (sample O5-1). In this domain also occur metamictic zircon included in moderately kaolinized microcline, Th-bearing monazite-(Ce), fluorite, and secondary Mn-Ba-oxides.

the perthite fraction of amazonite. Both occurrences of cassiterite from La Chinchilla are devoid of inclusions of other phases and neither evidenced any type of twinning. The content of SnO_2 of cassiterite 2 (Table 3, 4 analyses) varies from 93.2 to 96.4 wt.%; after Sn, Ca is the second most enriched element (1.14 to 1.24 wt.% CaO), followed by Ta_2O_5 and Nb_2O_5 (0.3 to 2.5 and 0.1 to 1.2 wt.%, respectively). The composition of cassiterite is completed by FeO_t (0.3 to 1.17 wt.%), TiO_2 (0.36 wt.% average), and minor or trace contents of other elements listed in Table 3. Manganese was undetectable or in extremely low amounts which results in a negligible Mn/(Mn+Fe^{2+}) ratio. The Ta/(Ta+Nb) ratio of metasomatic/hydrothermal cassiterite 5307 is slightly greater than 0.5, except for one analysis of 0.47.

In the $(Nb,Ta)^{5+}$–$(Fe,Mn)^{2+}$–$(Sn,Ti)^{4+}$ triangle (Fig. 9), cassiterite compositions of both samples are well correlated ($r^2 = 0.895$ and 0.984 for samples O5-1 and 5307, respectively, though both trends are barely distinguishable from each other). None of the analyses from either sample plot along the 2:1 ratio of the well known columbite coupled substitution type [$(Fe,Mn)^{2+} + 2(Ta,Nb)^{5+} = 3Sn + Ti^{4+}$] ("tapiolite" trend of Černý & Ercit 1985, 1989). Instead, both types of cassiterite better fit the 1:1 ratio substitution trend (much better for cassiterite 2 than for cassiterite 1), where the (Ta+Nb)/(Fe+Mn) ratios average 0.98 and 1.22, respectively, though some values of cassiterite 1 can be ~1.5. The 2:1 columbite substitution type, a mechanism of common widespread occurrence in pegmatitic and leucogranitic cassiterites (*e.g.*, Černý & Ercit 1985, 1989, Möller *et al.* 1988, Pal *et al.* 2007, Galliski *et al.* 2008, Llorens González *et al.* 2017) is not satisfied by either of the cassiterite types from La Chinchilla. Regarding cassiterite 2 of metasomatic-hydrothermal origin, a similar occurrence related to selective albitization of perthite is described by Pal *et al.* (2007) in pegmatites of the Bastar-Malkangiri Pegmatite Belt of Central India. At La Chinchilla, both cassiterite types largely overlap each other along the substitution vector, though that of sample O5-1 (cassiterite 1) is slightly more enriched in the M^{5+} and M^{2+} substituting components. The different paragenetic assemblages of each cassiterite type occurrence are also highlighted by the Ta#, which is very low in micropegmatitic cassiterite 1 (0.1 to 0.21), indicative of a largely Nb dominant cassiterite, quite different from that of hydrothermal cassiterite 2 (Ta#: ~0.47 to 0.57). It is noteworthy that, because of the high CaO contents of both cassiterite types (1.14 to 1.29 wt.% CaO) and considering that most of the available published data lacks Ca analyses, Ca becomes an expected component in this species. Recent data from Feng *et al.* (2019) shows an average of 0.56 wt.% CaO (averaged ranges from 0.49 to 0.59 wt.% CaO) from 50 EPMA analyses performed on nine samples from Li-, P-rich albite-spodumene pegmatites from the Kangxiwa–Dahongliutan Pegmatite Field in China. Other high CaO values were measured by Di *et al.* (2023) in cassiterite from muscovite granites (average 0.96 wt.% CaO; range from 0.91 to 1.05) and from associated quartz veins (average 1.02 wt.% CaO; range from 0.91 to 1.13) of the Xiangdong vein-hosted W-Sn deposit of South China.

Monazite-(Ce). Monazite related to miarolitic cavities in samples 5307b and O5-1 was identified through EDS analyses as Th-bearing monazite-(Ce). Included in a ~6 cm large amazonite crystal from a miarolitic cavity (sample 5307 b), it occurs as single grains or polygranular aggregates of anhedral to subhedral crystals from 0.2 up to ~0.8 mm included in aggregated laths of late albite that replaces amazonite in contact with millimeter-sized patches of fluorite (Fig. 6b). Here monazite-(Ce) was partially replaced by hydroxycalciopyrochlore that became enriched in P_2O_5, though not in LREE (Table 2). EDS analyses did not detect the presence of U.

Fluorite. Fluorite is conspicuous in miarolitic cavities from sampling points 5307 and T4 and in granitic samples H8-1 and O5-1. At La Chinchilla, none of the findings has so far provided idiomorphic crystals, where light purple fluorite exceptionally reaches a few centimeters in anhedral massive aggregates. EDS analyses of fluorite patches associated with albitization of amazonite and hydroxycalciopyrochlore + cassiterite (sample 5307) do not show elements present other than Ca and F, at least under EPMA detection conditions.

TABLE 3. ELECTRON MICROPROBE DATA (IN wt.%) OF CASSITERITE AND CALCULATED MINERAL FORMULAE AND ELEMENT RATIOS FROM LA CHINCHILLA MIAROLITIC AND MICROPEGMATITIC ASSEMBLAGES

Sample	5307B Cst 5	5307B Cst 6	5307B Cst 7	5307B Cst 8	O5-1 Cst 9	O5-1 Cst 10	O5-1 Cst 11	O5-1 Cst 12	O5-1 Cst 13	O5-1 Cst 14	O5-1 Cst 15	O5-1 Cst 16	O5-1 Cst 17
SnO_2	96.39	95.21	92.43	93.15	93.45	94.72	91.13	90.03	90.77	95.76	96.21	92.14	94.71
Ta_2O_5	0.31	1.25	2.49	2.07	0.61	0.44	1.31	1.40	0.94	0.34	0.19	1.23	0.72
Nb_2O_5	0.13	0.77	1.20	1.01	1.34	1.19	2.67	3.28	2.96	0.80	0.87	2.83	1.54
FeO	0.26	0.67	1.17	0.95	0.70	0.61	1.19	1.30	1.27	0.53	0.66	1.54	1.00
MnO	0.05	b.d.	0.07	0.07	b.d.	b.d.	0.07	0.09	b.d.	0.04	0.05	0.03	b.d.
MgO	0.10	0.07	0.08	0.06	0.09	0.10	0.03	0.06	0.09	0.02	0.09	0.06	0.06
TiO_2	0.39	0.36	0.34	0.34	0.27	0.30	0.38	0.44	0.40	0.28	0.54	0.45	0.29
SiO_2	0.02	0.01	0.00	0.04	0.05	0.09	0.01	0.06	0.04	0.03	0.02	0.08	0.09
WO_3	b.d.	0.14	0.08	0.11	0.10	0.00	0.19	0.09	b.d.	0.06	b.d.	0.15	0.03
ZrO_2	0.06	0.17	0.33	0.34	0.35	0.37	0.36	0.54	0.48	0.35	0.35	0.45	0.42
ThO_2	0.08	0.02	b.d.	0.04	0.06	b.d.	b.d.	0.06	b.d.	0.01	0.04	0.00	0.00
CaO	1.24	1.14	1.23	1.20	1.22	1.14	1.20	1.24	1.24	1.18	1.29	1.17	1.20
PbO	b.d.	0.06	0.06	b.d.	b.d.	b.d.	b.d.	b.d.	b.d.	b.d.	b.d.	b.d.	0.06
SrO	0.04	0.03	b.d.	b.d.	0.03	0.07	0.01	0.01	b.d.	b.d.	b.d.	b.d.	0.03
BaO	0.16	0.17	0.21	0.09	0.22	0.13	0.08	0.16	0.08	0.03	0.08	b.d.	0.09
Al_2O_3	0.05	0.04	0.03	0.05	0.06	0.03	0.06	0.01	0.03	0.04	0.02	0.02	0.03
Y_2O_3	b.d.	b.d.	0.01	b.d.	0.04	b.d.	0.02	b.d.	0.03	0.02	b.d.	b.d.	0.04
La_2O_3	b.d.	b.d.	b.d.	0.00	b.d.	b.d.	0.09	0.06	0.03	b.d.	0.02	0.03	0.03
Ce_2O_3	b.d.	0.05	0.07	0.06	b.d.	b.d.	0.06	0.11	0.02	b.d.	b.d.	0.01	0.16
Nd_2O_3	0.01	b.d.	0.03	0.11	0.02	0.10	0.09	b.d.	0.04	b.d.	0.07	0.03	b.d.
P_2O_5	b.d.	b.d.	b.d.	b.d.	b.d.	b.d.	b.d.	b.d.	b.d.	0.03	0.00	b.d.	0.01
Na_2O	0.04	0.05	b.d.	b.d.	0.00	b.d.	0.00	b.d.	b.d.	b.d.	0.01	0.04	0.02
F	0.13	0.05	b.d.	b.d.	b.d.	b.d.	b.d.	b.d.	b.d.	b.d.	b.d.	b.d.	b.d.
Total*	99.47	100.24	99.81	99.69	98.60	99.29	98.95	98.93	98.42	99.53	100.50	100.25	100.53

TABLE 3. CONTINUED.

Sample	5307B Cst 5	5307B Cst 6	5307B Cst 7	5307B Cst 8	O5-1 Cst 9	O5-1 Cst 10	O5-1 Cst 11	O5-1 Cst 12	O5-1 Cst 13	O5-1 Cst 14	O5-1 Cst 15	O5-1 Cst 16	O5-1 Cst 17
						Cation distribution on the basis of 2 O							
Sn	0.931	0.919	0.897	0.906	0.915	0.922	0.887	0.873	0.883	0.933	0.922	0.879	0.907
Ta	0.002	0.007	0.015	0.012	0.004	0.003	0.008	0.008	0.006	0.002	0.001	0.007	0.004
Nb	0.001	0.008	0.013	0.011	0.015	0.013	0.029	0.036	0.033	0.009	0.009	0.031	0.017
Fe	0.005	0.014	0.024	0.019	0.014	0.012	0.024	0.026	0.026	0.011	0.013	0.031	0.020
Mn	0.001	0.000	0.001	0.001	0.000	0.000	0.001	0.002	0.000	0.001	0.001	0.001	0.000
Mg	0.004	0.003	0.003	0.002	0.003	0.004	0.001	0.002	0.003	0.001	0.003	0.002	0.002
Ti	0.007	0.007	0.006	0.006	0.005	0.006	0.007	0.008	0.007	0.005	0.010	0.008	0.005
Si	0.001	0.000	0.000	0.001	0.001	0.002	0.000	0.001	0.001	0.001	0.000	0.002	0.002
W	0.000	0.001	0.001	0.001	0.001	0.000	0.001	0.001	0.000	0.000	0.000	0.001	0.000
Zr	0.001	0.002	0.004	0.004	0.004	0.004	0.004	0.006	0.006	0.004	0.004	0.005	0.005
Th	0.000	0.000	0.000	0.000	0.000	0.000	0.000	0.000	0.000	0.000	0.000	0.000	0.000
Ca	0.032	0.029	0.032	0.031	0.032	0.030	0.031	0.032	0.033	0.031	0.033	0.030	0.031
Pb	0.000	0.000	0.000	0.000	0.000	0.000	0.000	0.000	0.000	0.000	0.000	0.000	0.000
Sr	0.001	0.000	0.000	0.000	0.000	0.001	0.000	0.000	0.000	0.000	0.000	0.000	0.000
Ba	0.002	0.002	0.002	0.001	0.002	0.001	0.001	0.002	0.001	0.000	0.001	0.000	0.001
Al	0.001	0.001	0.001	0.002	0.002	0.001	0.002	0.000	0.001	0.001	0.001	0.001	0.001
Y	0.000	0.000	0.000	0.000	0.001	0.000	0.000	0.000	0.000	0.000	0.000	0.000	0.000
La	0.000	0.000	0.000	0.000	0.000	0.000	0.001	0.000	0.000	0.000	0.000	0.000	0.000
Ce	0.000	0.000	0.001	0.001	0.000	0.000	0.001	0.001	0.000	0.000	0.000	0.000	0.001
Nd	0.000	0.000	0.000	0.001	0.000	0.001	0.001	0.000	0.000	0.000	0.001	0.000	0.000
P	0.000	0.000	0.000	0.000	0.000	0.000	0.000	0.000	0.000	0.001	0.000	0.000	0.000
Na	0.002	0.003	0.000	0.000	0.000	0.000	0.000	0.000	0.000	0.000	0.000	0.002	0.001
F	0.010	0.004	0.000	0.000	0.000	0.000	0.000	0.000	0.000	0.000	0.000	0.000	0.000
Ta#	0.567	0.469	0.530	0.527	0.198	0.166	0.210	0.188	0.147	0.189	0.105	0.192	0.203
Mn#	0.169	0.000	0.053	0.065	0.000	0.000	0.058	0.067	0.000	0.069	0.074	0.022	0.000

b.d.: below detection limit.

* As, Sc, and K: analyzed but not detected.

Formula calculated on the basis of two cation charges.

Average formula: $(Sn_{0.94}Ca_{0.03}Ti_{0.01}Fe_{0.01})_{\Sigma 1.00}O_2$.

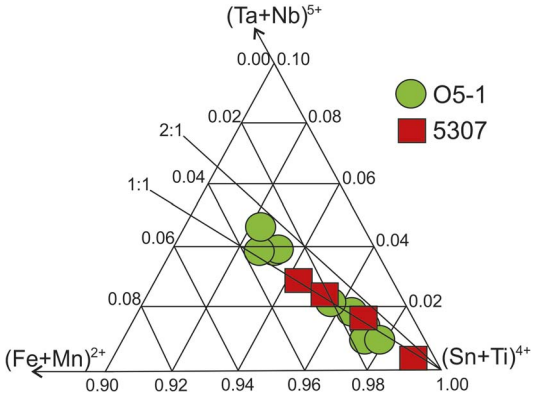

FIG. 9. M^{5+}–M^{2+}–M^{4+} triangle with the compositions of cassiterite samples O5-1 (primary micropegmatitic) and 5307 (secondary replacing phase); the 2:1 and 1:1 ratios represent the substitution trendlines of $Sn(+Ti)^{4+}$.

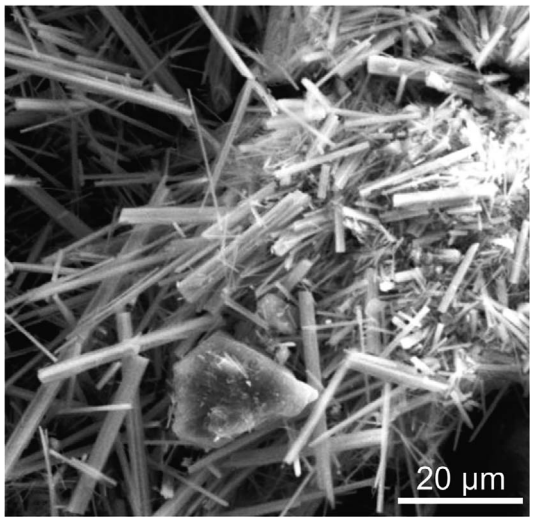

FIG. 10. SEM image of fine prismatic to fibrous carlosbarbosaite crystals from the T4 trench.

Mineralogy and mineral chemistry of carlosbarbosaite and paragenetic minerals in miarolitic cavities

Carlosbarbosaite. This new species, discovered in Jaguaraçu, Minas Geraes, Brasil (Atencio *et al.* 2012), of formula $(UO_2)_2Nb_2O_6(OH)_2 \cdot 2H_2O$, is the main uranium mineral at the La Chinchilla exploration prospect. Morello (2008, 2009, 2010, CNEA unpublished reports, 2013a) described the occurrence of carlosbarbosaite in the La Chinchilla porphyritic granite (T4 trench) as small crusts, coatings, or powdery aggregates (≤1mm) preferentially interstitial in "zinnwaldite" sheet cleavages, but also commonly filling cavities and microfractures in the granite, associated with coronadite, magnetite, hematite, zircon, Nb-bearing ilmenite, anatase, and fluorite. The aggregates originally described by Morello (2010, CNEA unpublished report, 2013a) were restudied in this work. These show pearly luster with a color varying from fading to intense yellow; individual crystals (~5 to 50 µm long) are transparent to translucent with a needle-like to fine prismatic habit (Fig. 10). Under the polarizing microscope, carlosbarbosaite is weakly pleochroic with anomalous birefringence. Under short- and long-wave ultraviolet radiation, carlosbarbosaite does not produce fluorescence. Debye-Scherrer diffractograms matched the compound identified as U-Nb-Ta-O, card # 29-1373 of the Mineral Powder Diffraction File 1993 (Morello 2010, CNEA unpublished report). X-ray data from carlosbarbosaite of the T4 trench, compared with other Argentinian occurrences and the Zapot mine (Foord *et al.* 1999), were published by Morello (2013a).

In this study we analyzed carlosbarbosaite from two different occurrences: a miarolitic pegmatite explored with the T4 trench and the porphyritic granite (sample 5031). Crystal aggregates of carlosbarbosaite from the T4 trench originated as a by-product of the pseudomorphic replacement of a primary miarolitic unidentified phase (likely a columbite group mineral, CGM) where it occurs in association with Nb-bearing hematite, muscovite, secondary quartz, and subordinate smectite group clay, likely montmorillonite (Fig. 11a to d). Two distinctive textural types of carlosbarbosaite do occur associated within the pseudomorphic assemblages: a well crystallized variety in radial and fan-shaped, fine prismatic (needle-like) aggregates where WDS analyses were performed and a micro- to cryptocrystalline network of dendritic intertwinned crystals (<1 to 15 µm) that under EDS analyses yield the same spectra as the coarser crystalline type. The micro- to cryptocrystalline type looks like an early growth stage of developing carlosbarbosaite (Fig. 11c–d). WDS analytical data of carlosbarbosaite from the T4 trench is presented in Table 4a; data were normalized to 14 anions and H_2O was calculated as by Atencio *et al.* (2012). Twenty-four spots from different patches of several replaced crystals were analyzed, six of which were discarded due to their low totals (<95 wt.% down to ~85 wt.% including calculated H_2O). The elements Na, Al, Th, and Pb were sought but were below the microprobe detection limits. No LREE peaks were detectable through EDS. Averaged data normalized to 14 anions resulted in the following empirical formula:

$$(Ca_{0.58}\square_{0.40}Mn_{0.02})_{\Sigma 1.00}[U_{1.39}\square_{0.61}O_{2.78}(H_2O)_{1.22}]$$
$$(Nb_{1.48}Ta_{0.06}Si_{0.35}Ti_{0.03}Fe_{0.08})_{\Sigma 2.00}O_{4.72}(OH)_{3.25}$$
$$(H_2O)_{2.03}.$$

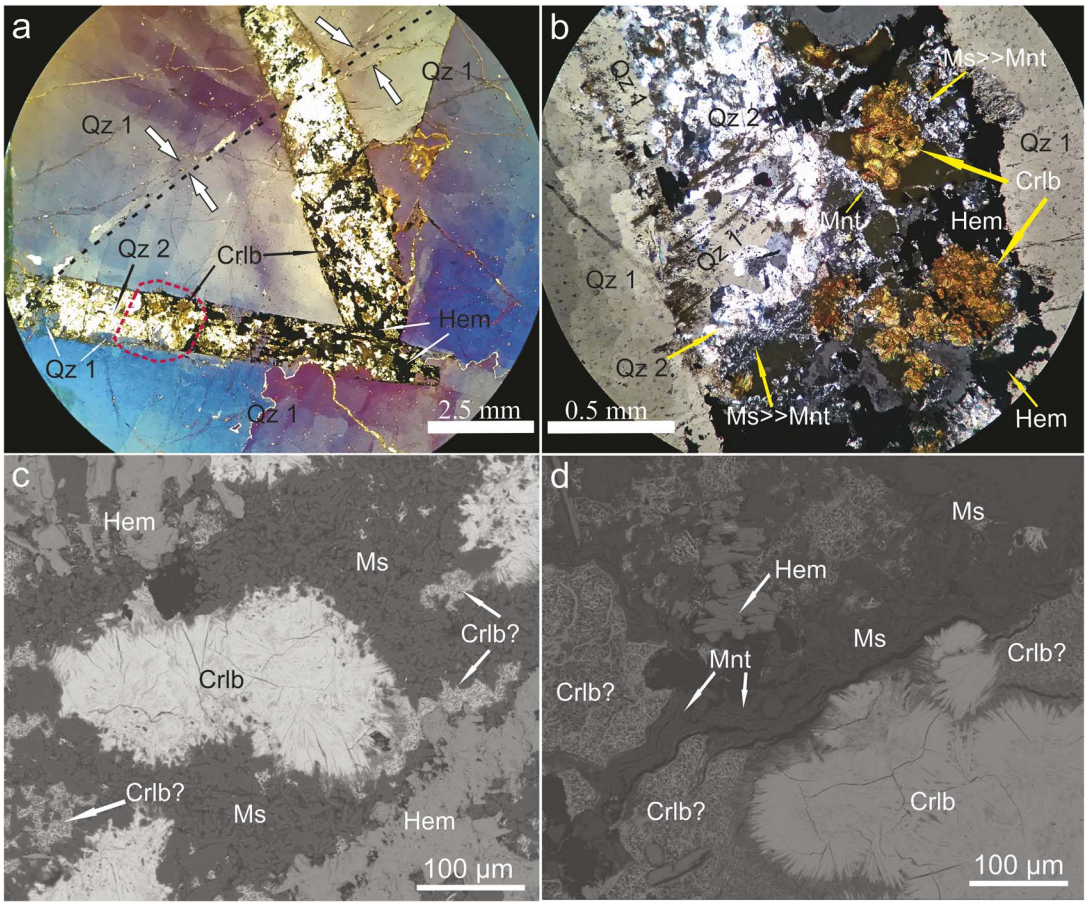

FIG. 11. (a) Unknown pseudomorphic crystals (possibly a CGM) included in cavity-filling smoky quartz (Qz 1). The crystals are totally replaced by aggregates of quartz (Qz 2) - hematite (Hem) - muscovite (Ms) - carlosbarbosaite (Crlb) ± a smectite group clay (likely montmorillonite, Mnt). Host and centripetal replacing quartz (Qz 1) normally shows large grains with undulose extinction and ribbon textured subdomains. Arrows point at a microfracture system that slightly separated the uppermost crystal into two pieces and crosscut the lowermost crystal; these microfractures locally host discontinuous quartz veinlets. Such an anastomosed network of microfractures was probably responsible for the fluid channeling and replacement processes of the CGM by Qz 2-Hem-Ms-Crlb-Mnt after smoky core quartz crystallization (Qz 1). Thin section = 30 µm, binocular stereoscopic microscope view under slightly crossed polarizers. (b) Close-up image of contoured area in (a) (crossed polarizers). (c–d) BSE images that show textural-paragenetic relationships among coarser-grained carlosbarbosaite (Crlb), probable cryptocrystalline carlosbarbosaite (Crlb?), and fine-grained muscovite (Ms) and smectite clay species (Mnt).

A comparison between the compositional ranges of the La Chinchilla carlosbarbosaite (T4 trench) and those from the Jaguaraçu type locality (Atencio *et al.* 2012) shows that the UO_3 contents of La Chinchilla (~48.5 to 55 wt.%; Fig. 12a–b) are within the range of samples 1 and 2 of Atencio *et al*. (2012). The CaO content, however, is enriched ~1.8 to >2 times the weight % registered in the Jaguaraçu samples (3.68–4.69 wt.%; Fig. 12b–c). A remarkable chemical difference between the two localities consists of the Nb_2O_5 and Ta_2O_5 values. The sum of both oxides averages 27.17 wt.% *versus* 29.36 (sample 1) to 31.08 wt.% (sample 2), but the Nb/(Nb+Ta) average ratio differs significantly from an average value of 0.96 (variable from 0.94 to 0.98) in the La Chinchilla samples down to a constant value of ~0.6 in the Jaguaraçu samples. This ratio places the La Chinchilla carlosbarbosaite as a strongly Nb-enriched member. Regarding the empirical formulae, the principal distinction of material from the type locality is in the relationship to the *Ca* site, which is dominated by Ca

TABLE 4A. SELECTED RESULTS OF ELECTRON MICROPROBE ANALYSES OF CARLOSBARBOSAITE (OXIDE IN wt.%) AND CALCULATED MINERAL FORMULAE AND ELEMENT RATIOS FROM LA CHINCHILLA MIAROLITIC PEGMATITE (T4 TRENCH)

Sample	O-U-Nb 1	O-U-Nb 2	O-U-Nb 3	O-U-Nb 4	O-U-Nb 5	O-U-Nb 6	O-U-Nb 7	O-U-Nb 9	O-U-Nb 10	O-U-Nb 11	O-U-Nb 13	O-U-Nb 15	O-U-Nb 16	O-U-Nb 17	O-U-Nb 18	O-U-Nb 19	O-U-Nb 20	O-U-Nb 23
UO_3	51.09	51.63	50.93	55.02	50.72	51.49	48.48	51.79	50.40	53.43	50.22	53.96	52.86	52.80	50.49	51.96	50.86	49.64
CaO	4.37	4.41	4.60	4.69	4.22	4.01	4.02	4.23	4.03	4.37	3.68	4.28	4.12	4.23	4.24	4.02	4.27	4.25
Nb_2O_5	26.41	26.17	25.70	27.24	25.53	26.84	25.65	26.27	24.83	25.97	24.47	24.71	24.39	26.34	25.29	23.99	24.23	26.09
Ta_2O_5	1.91	1.92	1.56	1.09	1.12	1.57	1.71	1.53	1.33	1.21	2.62	1.22	1.60	1.59	1.96	1.98	1.31	1.71
TiO_2	0.28	0.36	0.28	0.33	0.32	0.30	0.26	0.28	0.24	0.29	0.31	0.26	0.31	0.29	0.32	0.44	0.34	0.23
SiO_2	3.06	2.54	2.64	1.84	2.00	2.82	3.50	2.86	2.78	2.87	2.34	2.49	2.86	2.83	4.07	1.76	2.17	3.77
Fe_2O_3	0.69	0.85	1.10	1.02	1.01	0.77	0.69	0.88	0.78	0.73	0.85	0.76	0.85	1.10	1.22	0.79	1.15	0.59
MnO	0.19	0.11	0.20	0.16	0.17	0.12	0.18	0.20	0.19	0.23	0.17	0.12	0.13	0.11	0.16	0.30	0.25	0.20
H_2O*	12.36	11.62	11.68	10.56	10.54	12.16	12.89	11.93	10.99	10.82	9.78	10.58	11.96	13.74	9.33	10.23	13.17	10.82
Total**	100.37	99.62	98.69	101.94	95.63	100.08	97.38	99.98	95.58	95.48	97.58	97.70	101.25	101.49	94.57	94.81	99.65	95.48
Structural formula based on $\Sigma B = 2$																		
U	1.321	1.373	1.361	1.495	1.435	1.337	1.251	1.358	1.399	1.431	1.410	1.538	1.463	1.370	1.235	1.554	1.466	1.254
ΣU	1.321	1.373	1.361	1.495	1.435	1.337	1.251	1.358	1.399	1.431	1.410	1.538	1.463	1.370	1.235	1.554	1.466	1.254
Ca	0.576	0.598	0.627	0.650	0.609	0.531	0.529	0.566	0.571	0.596	0.526	0.621	0.581	0.559	0.528	0.612	0.627	0.547
Mn	0.020	0.012	0.021	0.017	0.020	0.013	0.019	0.022	0.022	0.025	0.019	0.014	0.014	0.012	0.015	0.036	0.029	0.020
ΣCa	0.596	0.610	0.648	0.667	0.629	0.544	0.548	0.587	0.592	0.621	0.545	0.635	0.595	0.570	0.544	0.649	0.656	0.567
Nb	1.469	1.497	1.478	1.592	1.555	1.500	1.424	1.482	1.483	1.495	1.476	1.514	1.451	1.469	1.329	1.542	1.500	1.417
Ta	0.064	0.066	0.054	0.038	0.041	0.053	0.057	0.052	0.048	0.042	0.095	0.045	0.057	0.053	0.062	0.077	0.049	0.056
Si	0.377	0.321	0.336	0.238	0.269	0.349	0.430	0.357	0.367	0.365	0.312	0.337	0.376	0.349	0.473	0.250	0.297	0.453
Ti	0.026	0.034	0.027	0.032	0.033	0.028	0.024	0.026	0.024	0.027	0.031	0.026	0.030	0.027	0.028	0.047	0.035	0.021
Fe	0.064	0.081	0.105	0.099	0.102	0.071	0.064	0.083	0.077	0.070	0.086	0.078	0.084	0.102	0.107	0.084	0.119	0.053
ΣB	2.000	2.000	2.000	2.000	2.000	2.000	2.000	2.000	2.000	2.000	2.000	2.000	2.000	2.000	2.000	2.000	2.000	2.000
Nb/(Nb+Ta)	0.958	0.958	0.965	0.977	0.974	0.966	0.961	0.966	0.969	0.973	0.939	0.971	0.962	0.965	0.955	0.953	0.969	0.962

* H_2O content calculated on the basis of 14 anions following the O:(OH):(H_2O) ratios assigned by Atencio *et al.* (2012).

** Na, Al, Th and Pb: analyzed but not detected.

Empirical formula for 18 averaged analyses: $(Ca_{0.58}\square_{0.40}Mn_{0.02})_{\Sigma 1.00}[U_{1.39}\square_{0.61}O_{2.78}(H_2O)_{1.22}](Nb_{1.48}Ta_{0.06}Si_{0.35}Ti_{0.03}Fe_{0.08})_{\Sigma 2.00}O_{4.72}(OH)_{3.25}(H_2O)_{2.03}$. Simplified formula: $(UO_2)_{1.40}[\square(H_2O)]_{0.60}Nb_2[O_{4.75}(OH)_{1.25}](OH)_2(H_2O)_2$.

TABLE 4B. SELECTED RESULTS OF ELECTRON MICROPROBE ANALYSES OF CARLOSBARBOSAITE (OXIDE IN wt.%) AND CALCULATED MINERAL FORMULAE AND ELEMENT RATIOS FROM LA CHINCHILLA PORPHYRITIC GRANITE (SAMPLE 5031)

Sample	5301-Pyr 7	5301-Pyr 9	5301-Pyr 11	5301-Pyr 12	5301-Pyr 13	5301-Pyr 15	5301-Pyr 16	5301-Pyr 18	5301-Pyr 20	5301-Pyr 21	5301-Pyr 22	5301-Pyr 23	5301-Pyr 24
UO_2	49.72	50.22	55.09	54.61	54.87	54.99	55.03	54.32	56.04	55.93	55.97	55.77	55.68
Na_2O	0.21	0.20	0.00	b.d.	b.d.	b.d.	b.d.	0.12	b.d.	b.d.	b.d.	0.01	b.d.
CaO	4.32	4.17	3.88	3.93	4.00	3.93	4.00	4.06	3.86	4.14	4.18	3.95	4.20
MnO	0.23	0.21	0.81	0.64	0.79	1.11	0.73	1.20	0.90	1.25	1.16	1.19	1.15
Fe_2O_3*	0.87	0.89	0.59	0.69	0.65	0.65	0.54	1.28	1.10	0.69	0.64	0.64	0.57
PbO	0.50	0.47	0.82	0.62	0.89	1.06	0.86	0.86	0.91	0.89	1.00	0.64	0.90
Y_2O_3	0.07	b.d.	0.06	0.04	0.05	0.01	b.d.	b.d.	0.03	0.03	0.03	b.d.	0.03
Ce_2O_3	0.23	0.20	0.27	0.17	0.24	0.11	0.23	0.23	0.14	0.16	0.16	0.21	0.17
Nd_2O_3	b.d.	b.d.	b.d.	b.d.	0.06	0.08	b.d.	b.d.	b.d.	b.d.	b.d.	b.d.	0.01
Sc_2O_3	0.03	0.04	0.04	b.d.	0.04	0.01	0.02	0.02	0.01	0.00	0.02	b.d.	b.d.
ThO_2	0.25	0.23	b.d.	b.d.	0.01	b.d.	0.05	0.02	0.07	b.d.	b.d.	0.05	b.d.
Ta_2O_5	7.35	7.13	4.24	4.70	4.21	3.63	3.83	2.69	4.18	2.16	2.65	3.15	1.72
Nb_2O_5	16.38	16.09	18.93	18.06	18.89	19.48	19.00	20.42	18.62	21.20	21.29	20.68	22.00
TiO_2	1.14	1.21	0.98	1.11	0.49	0.99	1.16	0.81	0.99	0.80	0.81	0.68	0.44
WO_6	6.03	5.66	6.03	6.60	6.43	4.72	4.65	4.86	5.96	4.27	4.56	4.62	4.95
As_2O_5	b.d.	0.05	b.d.	b.d.	b.d.	b.d.	0.05	0.03	b.d.	b.d.	0.02	b.d.	b.d.
P_2O_5	0.68	0.60	0.01	0.05	0.01	b.d.	0.04	0.03	b.d.	0.07	b.d.	b.d.	0.03
ZrO_2	0.21	0.31	0.18	0.22	0.15	0.19	0.16	0.16	0.23	0.14	0.15	0.13	0.12
MgO	0.10	0.04	0.02	0.01	0.01	0.02	0.04	0.00	0.01	0.06	0.04	0.05	0.02
Al_2O_3	0.57	0.46	0.09	0.12	0.12	0.07	0.16	0.12	0.10	0.09	0.08	0.05	0.12
SiO_2	1.25	1.15	0.59	0.73	0.71	0.57	0.78	0.53	0.57	0.43	0.40	0.49	0.53
F	0.00	0.48	0.39	0.18	0.32	0.21	0.32	0.33	0.14	0.63	0.26	0.42	0.26
K_2O	0.54	0.54	0.45	0.44	0.49	0.41	0.45	0.50	0.45	0.43	0.39	0.45	0.40
O=F	0.00	0.20	0.16	0.08	0.14	0.09	0.14	0.14	0.06	0.27	0.11	0.18	0.11
H_2O**	11.23	10.16	7.34	7.84	7.27	7.13	7.36	7.99	7.53	6.94	7.26	6.95	7.28
Total***	101.89	100.30	100.64	100.68	100.55	99.29	99.32	100.35	101.80	100.05	100.99	99.93	100.53

TABLE 4B. CONTINUED.

Sample	5301-Pyr 7	5301-Pyr 9	5301-Pyr 11	5301-Pyr 12	5301-Pyr 13	5301-Pyr 15	5301-Pyr 16	5301-Pyr 18	5301-Pyr 20	5301-Pyr 21	5301-Pyr 22	5301-Pyr 23	5301-Pyr 24
Structural formula based on $\Sigma B = 2$													
U	1.454	1.522	1.846	1.795	1.856	1.877	1.846	1.780	1.850	1.893	1.878	1.897	1.872
ΣU	1.454	1.522	1.846	1.795	1.856	1.877	1.846	1.780	1.850	1.893	1.878	1.897	1.872
Na	0.053	0.052	0.000	0.000	0.000	0.000	0.000	0.034	0.000	0.000	0.000	0.003	0.000
K	0.090	0.094	0.087	0.083	0.094	0.080	0.087	0.094	0.085	0.084	0.075	0.088	0.077
Ca	0.609	0.608	0.626	0.622	0.651	0.646	0.646	0.641	0.614	0.675	0.675	0.647	0.680
Mn	0.026	0.024	0.103	0.080	0.101	0.144	0.094	0.150	0.114	0.161	0.148	0.154	0.147
Pb	0.018	0.017	0.034	0.025	0.037	0.044	0.035	0.034	0.037	0.036	0.041	0.026	0.037
Y	0.005	0.000	0.005	0.003	0.004	0.001	0.000	0.002	0.002	0.002	0.000	0.002	0.004
Ce	0.011	0.010	0.015	0.009	0.014	0.006	0.013	0.008	0.009	0.009	0.011	0.009	0.012
Nd	0.000	0.000	0.000	0.000	0.003	0.004	0.000	0.000	0.000	0.000	0.000	0.000	0.000
Sc	0.003	0.004	0.006	0.000	0.005	0.001	0.003	0.000	0.000	0.000	0.000	0.000	0.001
Th	0.008	0.007	0.000	0.000	0.000	0.000	0.002	0.001	0.002	0.000	0.000	0.002	0.000
ΣCa	0.822	0.810	0.874	0.822	0.909	0.927	0.877	0.963	0.860	0.967	0.954	0.929	0.957
Ta	0.263	0.264	0.174	0.189	0.174	0.151	0.157	0.108	0.169	0.089	0.109	0.131	0.071
Nb	0.974	0.990	1.289	1.206	1.298	1.351	1.295	1.360	1.249	1.457	1.451	1.429	1.503
Ti	0.113	0.124	0.111	0.123	0.056	0.114	0.132	0.090	0.110	0.091	0.092	0.078	0.050
W	0.205	0.200	0.235	0.253	0.253	0.188	0.182	0.186	0.229	0.168	0.178	0.183	0.194
As	0.000	0.004	0.000	0.000	0.000	0.000	0.004	0.003	0.000	0.000	0.002	0.000	0.000
P	0.075	0.069	0.001	0.006	0.001	0.000	0.005	0.003	0.000	0.009	0.000	0.000	0.003
Zr	0.013	0.021	0.013	0.016	0.011	0.014	0.011	0.011	0.016	0.010	0.011	0.010	0.009
Mg	0.019	0.008	0.005	0.003	0.002	0.005	0.008	0.000	0.002	0.013	0.010	0.012	0.005
Al	0.088	0.074	0.016	0.021	0.022	0.013	0.029	0.020	0.017	0.017	0.014	0.010	0.021
Si	0.164	0.156	0.089	0.107	0.108	0.088	0.117	0.078	0.085	0.065	0.061	0.075	0.080
Fe^{3+}	0.086	0.091	0.067	0.077	0.074	0.075	0.061	0.142	0.123	0.079	0.072	0.073	0.064
ΣB	2.000	2.000	2.000	2.000	2.000	2.000	2.000	2.000	2.000	2.000	2.000	2.000	2.000
Nb/(Nb+Ta)	0.79	0.79	0.88	0.86	0.88	0.90	0.89	0.93	0.88	0.94	0.93	0.92	0.96

** H_2O content calculated on the basis of 14 anions following the O:(OH):(H_2O) ratios assigned by Atencio *et al.* (2012).

*** Sr, Sn, and Ba below detection limit.

Empirical formula for 13 averaged analyses: $(Ca_{0.64}\square_{0.10}Mn_{0.11}K_{0.09}Pb_{0.03}REE_{0.02}Na_{0.01})_{\Sigma 1.00}[U_{1.79}\square_{0.21}O_{3.58}(H_2O)_{0.42}](Nb_{1.29}W_{0.20}Ta_{0.16}Si_{0.10}Ti_{0.10}Fe_{0.08}Al_{0.03}P_{0.01}Zr_{0.01})_{\Sigma 2.00}O_{5.15}(OH_{2.49}F_{0.14})_{\Sigma 2.63}(H_2O)_{2.21}$.

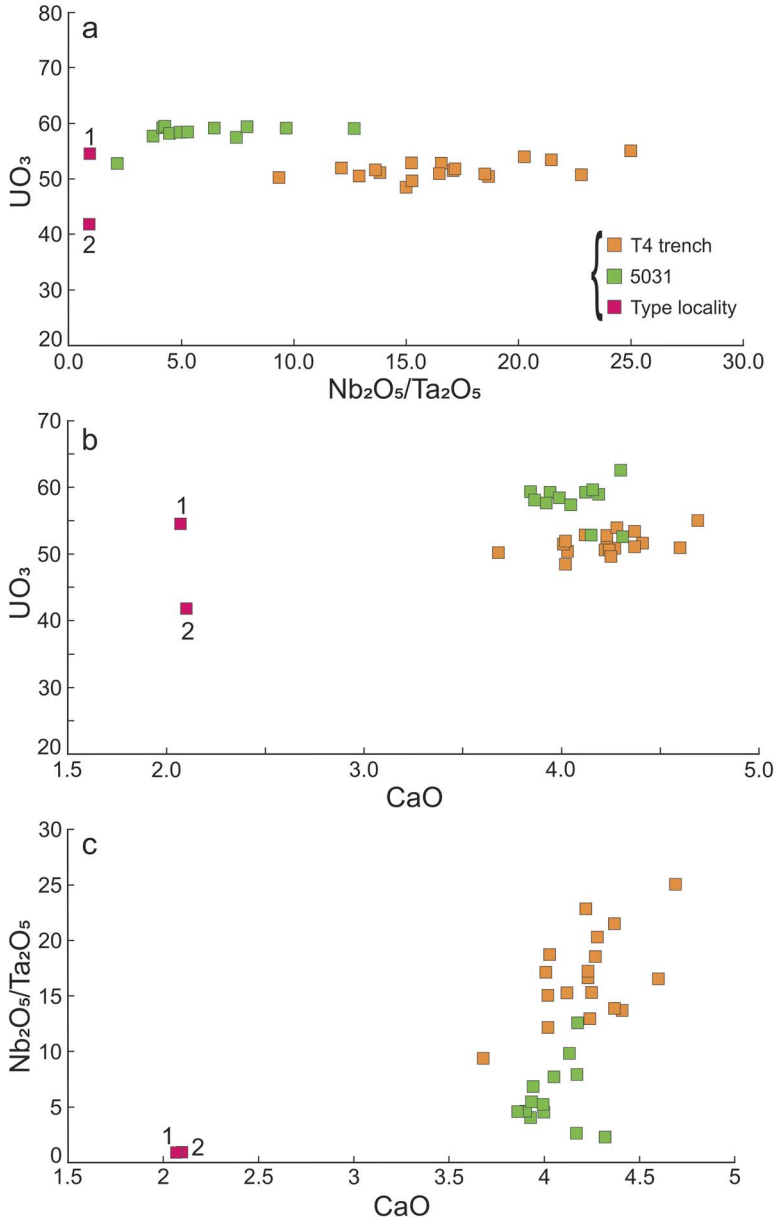

FIG. 12. Main cationic compositional ratios of indigenous carlosbarbosaite from La Chinchilla (T4 trench in sheared miarolitic pegmatite, $n = 18$, and sample 5031 from porphyritic granite, $n = 13$), compared to the average analyses of samples "1" ($n = 7$, U-bearing endmember) and "2" ($n = 7$, □-bearing endmember) from the type locality (Atencio *et al.* 2012). (a) U *versus* Nb/Ta showing Nb enrichment and the variability of the Nb/Ta ratios in the La Chinchilla carlosbarbosaite. (b) U *versus* Ca and (c) Ca *versus* Nb/Ta that evidence 1.8- to more than two-fold increase of the Ca content in the La Chinchilla samples.

(58%) instead of a vacancy (Jaguaraçu ≅ 67–68% □), whereas the *U* site is dominated by U^{6+} (69.5%) and the octahedral site by Nb^{5+} (74%), as it occurs in the Jaguaraçu samples. Regarding the variable amount of SiO_2 (1.76–4.07 wt.%) in the La Chinchilla analyses, its range acceptably overlaps the SiO_2 range of samples 1 and 2 from Jaguaraçu (2.02–3.79 wt.%). Si^{4+} was allocated in the octahedral site as hypothetically proposed by Atencio

et al. (2012), as was done with minor and variable quantities of Ti^{4+} (0.23–0.44 wt.% TiO_2) and Fe^{3+} (0.59–1.22 Fe_2O_3 wt.%). Traces of Mn^{2+} (0.11–0.30 wt.% MnO) were assigned to the *Ca* site (2% of the site). The U-bearing endmember in the formula represents X ≅ 0.7, hence the simplified formula of the T4 trench carlosbarbosaite can also be expressed as the ideal endmember $(UO_2)_2Nb_2O_6(OH)_2 \cdot 2H_2O$.

Analyzed carlosbarbosaite from sample 5031 occurs as a pseudomorphic replacement, likely after a PGS (pyrochlore group species) in the porphyritic granite, along the contact of polylithionite with feldspars (Fig. 13b). Thirteen WDS analyses of carlosbarbosaite from sample 5031 were selected from a total of 24 analyses (11 were discarded due to their low totals). The elements Sr, Sn, and Ba were also sought but not detected. Analytical data were processed as in Table 4a and presented in Table 4b. The empirical formula for 13 averaged analyses is $(Ca_{0.64}\square_{0.10}Mn_{0.11}K_{0.09}Pb_{0.03}REE_{0.02}Na_{0.01})_{\Sigma 1.00}[U_{1.79}\square_{0.21}O_{3.58}(H_2O)_{0.42}](Nb_{1.29}W_{0.20}Ta_{0.16}Si_{0.10}Ti_{0.10}Fe_{0.08}Al_{0.03}P_{0.01}Zr_{0.01})_{\Sigma 2.00}O_{5.15}(OH_{2.49}F_{0.14})_{\Sigma 2.63}(H_2O)_{2.21}$.

Carlosbarbosaite from sample 5031 yielded similar U and Ca contents to those of the T4 trench (~49.7 to 56 wt.% UO_3, 3.86 to 4.32 wt.% CaO, Fig. 12a–c). The sum of Nb_2O_5 and Ta_2O_5 averages ~23.28 wt.%, much lower than the average value of the T4 trench (27.17 wt.%), with Nb_2O_5 values within the 16.4 to 22 wt.% range and highly variable Ta_2O_5 contents ranging from 1.72 to 7.35 wt.%. The Nb/(Nb+Ta) ratio ranges from 0.79 to 0.96 (average 0.89), lower than the T4 trench ratios but still significantly higher than those of the type locality; these ratios also correspond to a Nb-enriched member (Fig. 12a–c). With reference to the empirical formula, the *Ca* site is dominated by Ca (64%), a reduced volume by vacancy (10%), and 26% of the site is assigned to several elements not detected in the T4 trench, neither reported for the Jaguaraçu samples, except for Ce and Nd [Mn > K > Pb > REE (Ce > Y > Nd) > Na]. The *U* site is controlled by U^{6+} (89.5%) and the octahedral site by Nb^{5+} (78.5%), as it occurs in the Jaguaraçu samples. Besides Nb, other elements that fill the octahedral site are W > Ta, Si ≅ Ti, Fe > Al > P ≅ Zr. The main distinguishing feature in this site is the presence of W in higher contents than Ta (WO_6 4.27 to 6.43 wt.%, average 5.3 wt.%). In reference to the SiO_2 contents, sample 5031 shows a significant drop compared to the T4 trench (range 0.4 to 1.25 wt.%, average 0.67 wt.%). The presence of trace quantities of several other elements not found in the type locality nor at the T4 trench does not affect the simplified formula of carlosbarbosaite from sample 5031 that can also be expressed as the ideal U-, Nb-rich endmember.

Hematite (Nb bearing). At the T4 trench, tabular aggregates of hematite (specularite variety) occur as a common pseudomorphic phase after the replacement of a probable CGM [likely columbite-(Fe)], associated with other secondary clay minerals and phyllosilicate species (a smectite group clay, likely montmorillonite), fine-grained muscovite (sericite), and carlosbarbosaite (Fig. 11). Hematite is Nb-bearing. The total Fe content

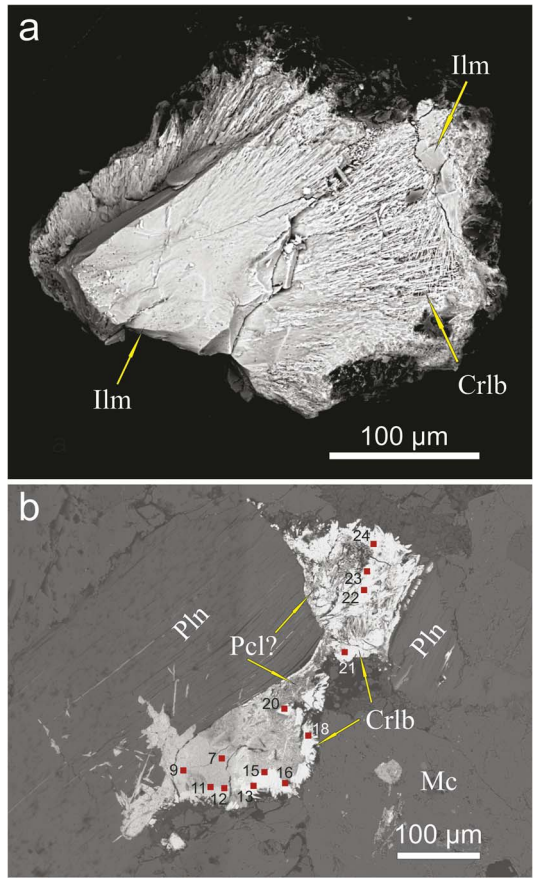

FIG. 13. (a) Nb-bearing ilmenite (Ilm) from the miarolitic cavity at the T4 trench, partially replaced by crisscrossed carlosbarbosaite (Crlb) fibers, originally named as "U-Nb-Ta oxide". Scanning electron microscopy image reproduced with permission of the Asociación Geológica Argentina, from Morello & Aparicio González (2013). (b) BSE image of carlosbarbosaite replacing a possible pyrochlore group species (Pcl?) from porphyritic granite (sample 5031). Pln – polylithionite, Mc – microcline. Numbered analyses 7 to 24 (n = 13) mark the analyzed spots listed in Table 4b. The lightest areas correspond to well-crystallized replacing carlosbarbosaite which yields the best totals and more uniform compositional range, whereas the darker gray zones gave low, unacceptable totals and more variable compositions on badly polished surfaces of finer-grained material with cracks typical of a metamictic phase (Pcl?).

TABLE 5. SELECTED ELECTRON MICROPROBE ANALYTICAL DATA OF Nb-BEARING HEMATITE (OXIDE IN wt.%) AND CALCULATED MINERAL FORMULAE FROM LA CHINCHILLA MIAROLITIC PEGMATITE (T4 TRENCH)

Sample	Hem 1	Hem 2	Hem 3	Hem 4	Hem 5	Hem 6	Hem 7	Hem 8	Hem 9	Hem 10
SiO_2	0.02	0.02	0.05	0.05	0.03	0.02	0.03	0.06	0.01	0.08
TiO_2	0.12	0.30	0.81	0.33	0.25	0.23	0.72	0.70	0.82	0.68
Al_2O_3	b.d.	0.03	0.06	0.17	b.d.	b.d.	0.01	0.08	0.19	0.24
Fe_2O_3	99.70	99.85	98.56	99.23	94.69	93.07	95.83	98.10	95.30	97.43
MnO	0.09	b.d.	0.07	0.06	0.24	0.46	0.10	0.08	0.22	0.23
Ta_2O_5	0.12	0.02	0.02	0.03	0.30	0.48	0.30	0.10	0.43	0.42
Nb_2O_5	0.46	0.35	0.13	0.08	4.14	5.63	1.94	0.15	2.66	1.07
Total	100.50	100.56	99.70	99.96	99.64	99.89	98.93	99.27	99.62	100.16
Si	0.000	0.000	0.001	0.001	0.001	0.001	0.001	0.002	0.000	0.002
Ti	0.001	0.003	0.008	0.003	0.002	0.002	0.007	0.007	0.008	0.007
Al	0.000	0.001	0.002	0.005	0.000	0.000	0.000	0.003	0.006	0.007
Fe	1.986	1.987	1.982	1.986	1.905	1.870	1.944	1.980	1.921	1.951
Mn	0.002	0.000	0.002	0.001	0.005	0.011	0.002	0.002	0.005	0.005
Ta	0.001	0.000	0.000	0.000	0.002	0.003	0.002	0.001	0.003	0.003
Nb	0.005	0.004	0.002	0.001	0.050	0.068	0.024	0.002	0.032	0.013

Formulae calculated on the basis of 3 cation charges: $(Fe_{1.95}Nb_{0.02}Ti_{0.01})_{\Sigma 1.98}O_3$.
Uranium analyzed but not detected.
n.d.: below detection limit.

as Fe^{3+} varies from 1.870 to 1.987 *apfu* (average 1.951), Nb *apfu* ranges from 0.001 to 0.068 (average 0.02), and traces of Ti, Ta, Al, Mn, and Si were detected; U was sought but not detected. The average formula of analyzed secondary hematite is $(Fe_{1.95}Nb_{0.02}Ti_{0.01})_{\Sigma 1.98}O_3$; Table 5, $n = 11$).

Muscovite. It occurs as fine-grained (<50 μm) sheet aggregates intergrown with all the other replacement phases (Fig. 11). However, detailed observations of textural relationships in thin section allowed us to distinguish that muscovite was deposited after quartz 2 and hematite and prior to carlosbarbosaite crystallization; its textural relationship with the probable montmorillonite is not clear. Electron microprobe analyses (Table 6) indicate that these hydrothermal micas are close in composition to the muscovite endmember, with high SiO_2 and Al^{VI} contents, poor Fe contents (2.5 to 3.9 wt.% FeO), and negligible amounts of Ti (from not detected to 0.08 wt.%) and <0.15 wt.% MnO; it is also poor in F (0.12 to 0.54 wt.%) and Li (0.02 to 0.17 wt.% Li_2O) contents.

Smectite group clay minerals. A species of the smectite group, likely montmorillonite, occurs as 20–30 μm-thick, elongated, fracture-filling wavy aggregates that deposited in contact with carlosbarbosaite, partially intergrown with fine-grained muscovite, prior to, though intimately related to, carlosbarbosaite formation (Fig. 11, Table 7). This smectite group clay is enriched in F (~1 wt.%) which likely replaces OH^- (*e.g.*, Thomas *et al.* 1977, Chipera & Bish 2002).

Discussion

Micropegmatitic-miarolitic granite evolution

Even though a fractional crystallization process could sustain some of the conclusions obtained here and by previous authors, a melt-melt-fluid immiscibility process could also explain the origin of common structural and textural features observable at the La Chinchilla pluton (miarolitic cavities, dikes, lenses; *e.g.*, Peretyazhko 2010, Thomas & Davidson 2014). For instance, the probable millions of micropegmatitic domains within the equigranular ≫ porphyritic granite could be the result of a failed process to permeate a pegmatite melt through the crystallized granite mush (Thomas *et al.* 2009, Thomas & Davidson 2014). A percolation cluster model at supersolidus conditions was proposed by Candela & Blevin (1995), who suggested that connectivity of magmatic volatile phase volumes was promoted by increasing volume proportions of the magmatic volatile phase (favored by initial water content of the magma and by decreasing *P*). With this model, the authors explained interconnected miarolitic textures that are enclosed in aplitic domains of the Ruby Creek and other shallow granites of Eastern Australia. It has been demonstrated that with cooling and as fractional crystallization proceeds, peraluminous F- and H_2O-rich granite magmas progressively enrich the residual melt with volatiles. When volatiles reach saturation, the melt may separate into two immiscible coupled melt

TABLE 6. RESULTS OF ELECTRON MICROPROBE ANALYSES OF MUSCOVITE (OXIDE IN wt.%) ASSOCIATED WITH HEMATITE-QUARTZ 2-SMECTITE CLAY GROUP-CARLOSBARBOSAITE, AND CALCULATED MINERAL FORMULAE FROM LA CHINCHILLA MIAROLITIC PEGMATITE (T4 TRENCH)

Sample	Crlbs Fil 4	Crlbs Fil 5	Crlbs Fil 6	Crlbs Fil 7	Crlbs Fil 8
SiO_2	47.90	49.68	50.72	49.44	47.43
TiO_2	0.08	0.02	b.d.	0.06	0.06
Al_2O_3	32.77	33.80	33.25	32.39	33.49
ZnO	0.26	0.22	0.23	0.15	0.17
FeO	2.52	2.51	2.64	3.86	2.55
MnO	0.09	0.03	0.14	0.20	0.06
MgO	0.71	0.64	0.97	0.52	0.44
CaO	0.20	0.17	0.24	0.15	0.13
BaO	b.d.	b.d.	b.d.	0.01	b.d.
Na_2O	0.06	0.04	0.07	0.02	0.05
K_2O	9.20	8.78	8.83	9.37	9.41
F	0.54	0.12	0.37	0.32	0.30
Cl	b.d.	0.01	b.d.	0.01	0.01
Li_2O*	0.17	0.02	0.11	0.09	0.08
H_2O**	4.21	4.52	4.46	4.39	4.31
Total	98.70	100.57	102.05	100.97	98.50
O=F.Cl	0.23	0.05	0.16	0.14	0.13
Total	98.48	100.51	101.89	100.83	98.37
Si	6.435	6.496	6.550	6.519	6.382
Al(IV)	1.565	1.504	1.450	1.481	1.618
ΣT	8.000	8.000	8.000	8.000	8.000
Al(VI)	3.623	3.705	3.611	3.553	3.694
Ti	0.008	0.002	0.000	0.006	0.006
Zn	0.026	0.021	0.022	0.014	0.017
Fe	0.283	0.274	0.285	0.426	0.287
Mn	0.010	0.003	0.016	0.022	0.007
Mg	0.142	0.124	0.188	0.102	0.089
Li	0.094	0.013	0.055	0.045	0.044
ΣM	4.186	4.144	4.177	4.168	4.145
Ca	0.029	0.023	0.033	0.021	0.019
Ba	0.000	0.000	0.000	0.001	0.000
Na	0.015	0.009	0.017	0.005	0.012
K	1.577	1.465	1.455	1.576	1.615
ΣA	1.621	1.497	1.506	1.602	1.646

* Li_2O calculated after the equation $Li_2O = 0.3935 * F^{1.326}$ proposed by Tischendorf *et al.* (2004).
** H_2O content calculated on the basis of charge balance.
Total iron expressed as Fe^{2+}.
b.d.: below detection limit.

fractions, one that evolves into increasing peraluminosity and the other into increasing peralkalinity (Thomas *et al.* 2006). The water concentration of the peralkaline melt fraction can increase up to 50 mass % H_2O and produce large volume changes (*i.e.*, the Königshain miarolitic pegmatites, Thomas *et al.* 2006, 2009, Rickers *et al.* 2006). Below ~600 °C these melts will transitionally shift into a fluid-dominated system, where strong *P* fluctuations are feasible, as a consequence of phase transformations such as OH^- and CO_3^{2-} in the melt exsolving into molecular H_2O and CO_2 (Thomas *et al.* 2009). At La Chinchilla, the notorious rupture of the largest miarolitic cavities (*e.g.*, >0.3 to <1.0 m in size) suggests that critical fluid overpressure might have locally exceeded the confining pressure, partially favored by shallow emplacement. Another alternative might be that possible differential internal fluid pressures ($\neq$ pressure gradient) among the neighboring pockets, likely originally interconnected, could have induced fracturing of pockets and "fluid explosions," as described by Peretyazhko *et al*. (2004) in the Oktaybrskaya pegmatite, central Transbaikalia.

TABLE 7. ELECTRON MICROPROBE ANALYTICAL DATA (OXIDE IN wt.%) OF FLUORINE-RICH SMECTITE GROUP CLAY (LIKELY MONTMORILLONITE), AND CALCULATED MINERAL FORMULAE FROM LA CHINCHILLA (T4 TRENCH)

Sample	Fil 1	Fil 2	Fil 3
SiO_2	50.14	49.71	52.18
TiO_2	0.01	0.02	b.d.
Al_2O_3	16.42	15.74	16.97
ZnO	0.67	0.63	0.76
FeO	3.11	3.39	3.11
MnO	0.11	0.10	0.13
MgO	3.74	3.52	4.00
CaO	0.95	0.96	1.11
Na_2O	0.11	0.11	0.12
K_2O	2.48	2.21	1.93
BaO	0.05	0.00	0.14
F	1.00	1.03	1.11
Cl	0.04	0.03	0.03
Total	78.82	77.44	81.60
O=F.Cl	0.43	0.44	0.47
Total*	78.39	77.00	81.12
Cation distribution on the basis of 22 O			
Si	7.834	7.899	7.852
$Al^{(IV)}$	0.166	0.101	0.148
$Al^{(VI)}$	2.857	2.847	2.862
Ti	0.001	0.002	0.000
Zn	0.078	0.074	0.085
Fe	0.406	0.451	0.391
Mn	0.015	0.013	0.017
Mg	0.871	0.834	0.897
Ca	0.160	0.163	0.179
Na	0.032	0.033	0.036
K	0.494	0.448	0.371
Ba	0.003	0.000	0.008
L. charge	0.425	0.403	0.390
I. charge	0.425	0.403	0.390

* H_2O^-: not measured.
Total iron expressed as Fe^{2+}.

HFSE in granites and miarolitic pegmatites

The two main granite types and subordinated units or facies from La Chichilla pluton represent small batches of strongly specialized magmas whose most remarkable feature is the extraordinary amount of seriate miarolitic NYF pegmatites from micrometer- to meter-scale sizes, dominantly in the equigranular body, which indicates low P (<2 kbar) crystallizing melts. HFSE-bearing phases (particularly Nb, Ta, U, Ti, Zr, Th) and fluorite are accessory minerals related to the latest stages of magmatic differentiation of both granites, preferentially associated with late crystallizing siderophyllite, smoky quartz, and albite of the initializing micropegmatitic stage. The experimental partitioning data between granite melts and coexisting fluids presented by Borodulin *et al*. (2009) demonstrates that with decreasing T, Nb and particularly Ta are retained in the melt until the final stage of melt-fluid interaction and may concentrate and crystallize Nb-Ta phases directly from the silicate melt. These experimental results could satisfactorily explain the ubiquitous crystallization of accessory HFSE-bearing phases such as columbite-(Fe), fergusonite, betafite group phases, monazite-(Ce), and others included in late crystallizing Li-micas of the siderophyllite–protolithionite series, and also in polylithionite, smoky quartz and albite during the late stages of micromiarolitic–miarolitic pegmatite evolution. The subsequent metasomatic and hydrothermal alteration processes addressed by Borodulin *et al*. (2009) would lead to the dissolution of late-magmatic Nb-Ta species and redeposition in other parts of the granite system. This alteration-replacement stage might be relevant to the formation stage of PGS after earlier HFSE-minerals as found in La Chinchilla. It is equally consistent with the conclusions of Badanina *et al*. (2010) from their investigation of the trace and REE composition of "columbite–tantalite" from the Orlovka massif in Eastern Transbaikalia, which suggested that crystallization of this CGM occurred at the late magmatic stage. From experimental work within the range 650–850 °C and 0.3 to 4 kbar, Chevychelov *et al.* (2010) also suggested that columbite crystallization was possible at final near-solidus stages during the high degrees of crystallization of strongly evolved low-T melts. They found that the maximum columbite solubility is reached in peralkaline melts, wherein the maximum contents of Ta and Nb are at least one order of magnitude lower in subaluminous and peraluminous melts, whereas the peralkaline melt is relatively enriched in Nb and the peraluminous melt is enriched in Ta. At liquidus and above-solidus conditions, Nb and Ta are concentrated in the residual melt of rare metal Li-F granites, do not partition into the aqueous fluid, and are incompatible with early crystallizing phases (Shapovalov *et al*. 2019). With decreasing T, Ta and Nb are strongly partitioned into the granite melt enriching their concentrations in equilibrium with fluorine-bearing fluids ($^{fluid/melt}D_{Nb,Ta} = 0.001–0.022$). The strong correlation between HFSE (*i.e.*, Ti, Nb, Ta, Zr, Hf, Th, U) and F (*e.g.*, Keppler 1993, Demartis *et al.* 2014, Lukyanova *et al.* 2017) can be explained by the highly incompatible behavior of many HFSE in the presence of F in granitic systems that evolved by differentiation from a common magma source. The experimental data of Zaraisky *et al*. (2010) demonstrate that Ta and Nb can be transferred to a hydrothermal fluid *via* concentrated fluoride solutions (mainly as HF) within the P-T range of 300–550 °C and 0.5 to 1 kbar. Lukyanova *et al.* (2017) arrived at the same conclusion with similar P-T conditions, considering the neutralization

of F-acidic solutions or a decrease of F concentration as the most likely causes of Nb-Ta-oxide precipitation, while decreasing *P-T* conditions were apparently of subordinate incidence. At La Chinchilla we should not underestimate, as well, the enhancement effect that could have contributed a progressive enrichment in Na. The strong genetic link between HFSE mineralization and late stage albitization process in granitic systems (*i.e.*, localized late redistribution of Na within a granitoid body) is well known (*e.g.*, Beus *et al.* 1962, Kinnaird 1984, Schwartz 1992).

Late- to postmiarolitic-hydrothermal stage

Hydrothermal fluids played an important role as rare metal carriers during the latest stages of miarolitic pegmatite and pocket formation. This stage was characterized by Na-, F-, and Li-enrichment in the form of replacement and vug-filling overgrowths of albite (cleavelandite), fluorite, and extremely F-rich polylithionite. Fluorine enrichment during late- to postmagmatic processes is a well documented process worldwide; it has been proven to be crucial for the release and mobilization of HFSE, REE, and Ti from primary magmatic species (*i.e.*, Jiang *et al.* 2003). Similarly, Jiang *et al*. (2005) emphasized that the mobility of HFSE in hydrothermal systems, particularly of Zr, Hf, and Ti, but also of Nb and Ta, was enhanced by high pH conditions and increasing F activity. In the same way, Linnen *et al*. (2012) highlighted the importance of F as a rare metal carrier in hydrothermal fluids and related mineralization, particularly in NYF pegmatites. In terms of mass balance, the availability of F during the late-miarolitic to hydrothermal stage at La Chinchilla was enhanced by the subsolidus phengitization process of magmatic micas of the siderophyllite–protolithionite series, which put into solution considerable amounts of F (and Li) during the replacement process, thus likely incorporating more F (and Li) in the residual original concentration derived from high *T* magmatic fractionation (Lira *et al*. 2023, unpublished).

Replacements of U-bearing hydroxycalciopyrochlore (± Nb-bearing cassiterite) after an unknown species and of P-enriched hydroxycalciopyrochlore to hydroxycalciomicrolite after monazite-(Ce), all did crystallize from Na-, F-enriched fluids. The chemical reaction of hydroxycalciopyrochlore type 2 partially replacing monazite-(Ce) illustrated in Figure 6b is not fully discerned upon element redistribution because even the new formed PGS is P-enriched, the incorporation of major LREE and Th is not evident, and any other secondary species counting for those elements has been recorded. Equal attention should be addressed to the presence of U in hydroxycalciopyrochlore type 2, considering that U was not detected in monazite-(Ce). Hence, one plausible interpretation is that monazite-(Ce) was originally intergrown with a U-bearing CGM and that the observed replacement reflects a complete and selective transformation of the CGM, while monazite was only affected by marginal replacement. The other interpretation depends on the presence of Nb and U in the Na-F-rich fluid.

An evolving trend indicated by increasing Ta# (Ta/Ta+Nb) with slightly decreasing Ti seems to be representative of the postmiarolitic evolutionary stage, as shown by the evolving composition of late-forming hydroxycalciopyrochlore that gradually becomes hydroxycalciomicrolite by entering the microlite field. The Ta# [Ta/(Ta+Nb)] in cassiterite also helps in understanding the evolution of the system from less evolved micromiarolitic assemblages within granite (sample O5-1) toward more evolved late- to post-miarolitic fluid-rich stages in decimeter- to meter-sized pegmatite pockets (sample 5307), which notably increased from 0.1–0.2 to ≥0.5 in the latter. The source of Ta was not investigated, however, the most likely source of released Ta could have been micas of the siderophyllite–polylithionite series during muscovitization (Li-bearing phengite). The variation of the Ta# in PGS and cassiterite suggests a fractionation process between Nb and Ta at low hydrothermal temperatures, which is highly dependent on the variation of the pH (Friis & Casey 2018). The Ta# of oxides increases with alkalinity in Na-rich domains (*i.e.*, replacing cleavelandite). The generation of metasomatic-hydrothermal albite below 2 kbar could be due to the leak of a cooling volatile aqueous fluoride-enriched fluid after miarolitic cavity rupturing due to internal fluid overpressure (Laurs *et al.* 1998 and citations therein). Peretyazhko & Zagorsky (2002) concluded that the bursting pressure release during the opening of miarolitic cavities often induced the boiling of fluids, changing their composition and generating dissolution, recrystallization, new mineral formation in vugs, and metasomatic alteration by interaction of residual fluids with the already crystallized pegmatite matrix. The remarkable whitish rim of amazonite crystals irregularly depleted in Pb content (*e.g.*, sample 5307; Lira *et al.* 2015), interpreted as due to a centripetal bleaching process by Martin *et al*. (2008) in amazonites from Madagascar, might also be due to fluid release after pocket rupture. It is also well known that late stage F enrichment in the melt will strengthen Na-metasomatism (albitization) by shifting the granite minimum melt toward albite composition and, hence, result in the separation of a metasomatic-hydrothermal fluid with a higher Na/K ratio (*e.g.*, Manning 1981). Though more recent studies have interpreted late magmatic albitization as the result of unmixing between Na-F-rich hydrosaline melts and K-rich aluminosilicate melts (*e.g.*, Badanina *et al.* 2004) and after melt-melt-fluid immiscibility (Müller *et al.* 2018), it does not seem to be appropriate for our study case. At La Chinchilla, replacement albite evidently

originated after interaction of a late granitic, Na-enriched fluid with crystallized granitic/pegmatitic feldspars (*e.g.*, Engvik *et al.* 2008). Progressive enrichment of Sn during melt differentiation by fractional crystallization until the precipitation stage of cassiterite during early micromiarolitic and late-miarolitic stages would have likely been feasible due to rising concentrations of H_2O and particularly of F. Both volatiles could have decreased the viscosity and increased the diffusivity in the melts in addition to the formation of various stable fluoride complexes in the melt and coexisting fluids, as demonstrated through melt/fluid inclusion studies (*e.g.*, Thomas *et al.* 2005, Thomas & Davidson 2013). At La Chinchilla, F was readily available from the melt stage (*e.g.*, 0.35 wt.% F in a whole-rock porphyritic sample) to the hydrothermal/supergene mineralization environment, as is particularly evident at the T4 trench sheared pegmatite zone, where F-bearing smectite group clays (likely montmorillonite, ~1 wt.% F) occur in intimate association with indigenous carlosbarbosaite (*i.e.*, carlosbarbosaite formed by the direct replacement of an *in situ* previous Nb-bearing species, to distinguish it from "transported" carlosbarbosaite, which precipitates distanced from the Nb source).

Genesis of carlosbarbosaite

Atencio *et al*. (2012) described the occurrence of carlosbarbosaite at the Jaguaraçu pegmatite type locality as a late stage cavity-filling species in albite, in close association with zircon, muscovite, kaolinite, and columbite-(Fe). These authors also recognized as probable carlosbarbosaite a supergene species described by Abd El-Naby (2008) in the Eastern Desert of Egypt, and other previous findings in pegmatites from Cerro Blanco, Tanti, Córdoba, Argentina (Arcidiácono 1974, Arcidiácono & Bedlivy 1976a, b). Morello (2013a) and Morello & Aparicio González (2013) described an unknown species from the La Chinchilla granite that was later recognized as carlosbarbosaite (Morello 2013b). Morello (2013b) pointed out that a few occurrences previously described from other regions of the world also matched that of carlosbarbosaite, *i.e.*, Foord *et al*. (1999) in Mineral County, Nevada, USA, and Saulnier & Morello (2002), in San Ignacio-Cumbre de los Pinos (Catamarca and Tucumán provinces, Argentina). Saulnier & Morello (2002) described their finding in a granitic pegmatite body as thin alteration coatings on "columbite–tantalite"; they also mentioned that the "U-Nb-Ta mineral" (*i.e.*, carlosbarbosaite) occasionally occurs as an apparent pseudomorphic replacement of possible "pyrochlore" and as freely crystallized aggregates interlayered between mica sheets. Recently, Anzil *et al*. (2022) described the occurrence of carlosbarbosaite replacing "columbite and tantalite", and filling voids and biotite cleavages, in another neighboring Carboniferous pluton of the NE region of the Velasco ranges (the Piedra Pintada or the La Punta pluton).

At La Chinchilla, Bardelli *et al*. (2018) identified two main modes of occurrence of carlosbarbosaite: (1) disseminated in the porphyritic granite facies and (2) concentrated in the border zone of a large miarolitic cavity in the T4 trench. In both occurrences, its origin was interpreted as a weathering product of primary granitic accessory phases: ["oxyuranopyrochlore" and columbite-(Fe)] in the first type, and after the pseudomorphic replacement of an unknown species [likely columbite-(Fe)] in the second type. In this study we confirm that carlosbarbosaite, in a partial replacement reaction of columbite-(Fe) of mode of occurrence (1) (*i.e.*, sample WP195) was mistakenly defined as accessory "oxyuranopyrochlore" by Bardelli *et al*. (2018), an erroneously used term in the sense of "uranopyrochlore" from Atencio *et al.* (2010); in fact, actually neither term is accepted by the IMA. The term "oxyuranopyrochlore" represents a theoretical U-rich endmember pyrochlore group species ($\square UNb_2O_6O$), proposed to form a hypothetic solid solution with the possible new species "oxyuranobetafite" [$(\square_{0.5}U_{1.5})_2Ti_2O_6O$; Mokhov *et al.* 2008, Matyszczak 2018, Atencio 2021]. Carlosbarbosaite replacing columbite-(Fe) from sample WP195 occurs included in late phengitic muscovite that contours micropegmatitic assemblages and in smoky quartz of the porphyritic granite facies. Magmatic columbite-(Fe) was classified based on the high Nb/(Nb+Ta) and Fe/(Fe+Mn) ratios, derived through EDS analyses (Bardelli *et al.* 2018).

A common observation of Bardelli *et al*. (2018) is that carlosbarbosaite occurs as a replacement phase of earlier crystallized Nb minerals or, otherwise, as precipitated coatings or cavity-filling aggregates near the Nb source. This was confirmed for disseminated carlosbarbosaite in the normal granite facies that crystallized as a pseudomorphic phase or precipitated at micro- to millimetric distances from PGS and columbite-(Fe) grains. In this sense, carlosbarbosaite distribution mimics the random distribution of some of the granite PGS and CGM accessory phases. The alteration of members of the pyrochlore group by low to high *T* hydrothermal fluids and by supergenic fluids is well documented. The process is frequently favored by metamictization operated by several substitution mechanisms (*e.g.*, Lumpkin & Ewing 1995 and references therein, Wall *et al.* 1996, Nasraoui *et al.* 1999, Nasraoui & Bilal 2000, Geisler *et al.* 2004, Zaitsev *et al.* 2012). Besides dissemination, the second mode of occurrence of carlosbarbosaite described by Bardelli *et al*. (2018) was at the external zone of a miarolitic pegmatite cut by the T4 trench. The authors distinguished groups of unknown idiomorphic crystals completely transformed into aggregates of quartz-

hematite-carlosbarbosaite-unidentified phases (their Figure 7). The miarolitic pegmatite is traversed by a brittle fault zone that produced brecciation and favored supergene hydrolysis (strong argillitization and oxidation) of both the pegmatite and enclosing porphyritic granite mineral assemblages. It seems that under these conditions some of the primary Nb-Ta-Ti-(±U?) oxide phases were partially or totally dissolved and the soluble compounds were transported farther distances (though within a couple of meters), also probably favored by enhanced permeability due to brecciation.

In this contribution we completed the study of Bardelli *et al*. (2018) identifying, moreover, a smectite group species and fine-grained muscovite and providing WDS analyses of all the pseudomorphic components (Fig. 11, Tables 5, 6, and 7). The completely replaced species (no relics were found) occur in prismatic individual crystals up to 1.5 cm long (1 mm thick), included in smoky quartz of the outer zone of the pegmatitic core; some of these crystals are rooted in strongly altered and leached K-feldspar. Idiomorphism of all unknown crystals suggests an orthorhombic or less probable monoclinic symmetry, though not confirmed. Its habit also permits the exclusion of PGS as the primary phase, unless a PGS had earlier replaced a previous species, as in the mineral association described for sample 5307. However, an elementary mass balance calculation does not support the resulting secondary mineral association as a pseudomorphic replacement product of a pyrochlore supergroup species. The most plausible candidate as a primary species would be a member of the CGM, most likely columbite-(Fe). Though variable, an average mineral composition of the replacing association is Nb-bearing hematite (30–40%), quartz (30–50%), carlosbarbosaite (5–15%), muscovite (<10%), and smectite group species (~5%). Silicification occurs in two modes: (1) as large grains grown from the host smoky quartz and in optical continuity with it, replacing the possible CGM in a centripetal mode (Qz 1), or (2) as polygranular patches of smaller quartz grains (Qz 2, mosaic texture) within the replaced CGM host. The whole amount of replacing quartz 1 and 2 can reach ~50% volume, in some sectors resembling ghost crystals whose borders are delineated by hairlines within the massive smoky quartz (Fig. 11a–b).

Any consideration of replacement leads to the need to invoke reactions with late fluids. Host quartz shows undulatory extinction and grain subdomains, as well as numerous fluid inclusion-rich microfractures that crosscut the possible CGM crystals, suggesting intense fluid activity during the hydrothermal stage of miarolitic evolution. The formation of Nb-bearing hematite and carlosbarbosaite could account, at least partially, for immobile Nb (±Ta) preserved from the source, though most U and other elements present in carlosbarbosaite and in the other associated silicates (*i.e.*, Al, K, Mg, Ca) were most likely related to the latest stages of strong silicification, and even later, at much lower *T*. Pseudomorphic hematite occurs in euhedral tabular [0001] crystals mostly oriented with their longest dimensions parallel to the elongation of the CGM crystals, intergrown with quartz 2 in apparent equilibrium with fine-grained muscovite (Fig. 11b, c, d). However, carlosbarbosaite formed later than the hematite-quartz-muscovite assemblage, filling intergranular voids or intimately intergrown with "smectite clay" aggregates and Fe-oxides/hydroxides derived from hematite alteration.

We are unable to demonstrate in which thermal interval carlosbarbosaite and clays did precipitate. The fact that these pseudomorphs are practically occluded in quartz and without any evidence of interaction with supergene fluids supports a low-*T* hydrothermal origin for this occurrence type of carlosbarbosaite, namely indigenous.

At the same locality (T4 trench), Morello (2013a) and Morello & Aparicio González (2013) found evidence of another example of pseudomorphic replacement of carlosbarbosaite after Nb-, Ta-bearing ilmenite (Fig. 13a), with secondary anatase as a probable by-product of the replacement reaction. EDS analyses did not detect any U traces in ilmenite, and likewise, we have no proof that U was present in the probable CGM; this fact favors the interpretation that U could have come into solution with the silica-rich alteration/replacing fluids to form a type of indigenous carlosbarbosaite, after entering in contact with a readily reactive CGM. In fact, silica-rich U-bearing fluids were relatively common in the surroundings, as is evidenced by the presence of fracture-filling uranophane associated with botryoidal silica in a few sites in the La Chinchilla body, particularly where desilicification was important, such as in some episyenite bodies (Morello 2009, unpublished report; Colombo 2014, *pers. commun.*; Bardelli *et al*. 2018).

Pseudomorphic indigenous carlosbarbosaite also occurs as a replacement phase of an unknown species that only survives as relic metamictic features (sample 5031 from porphyritic granite, Fig. 13b). As interpreted from the composition of replacive carlosbarbosaite from this sample (Table 4b), particularly of the cations hosted in the *A* site (K-Pb-REE-Na), subordinately in the *B* site (W-P-Zr), and of F in the *Y* site, this could likely feature a complete replacement of a PGS precursor, whose original composition looks quite different in terms of minor cations from the already described hydroxycalciopyrochlores from sample 5307, particularly its notorious enrichment in W. In this example, as in any other in which carlosbarbosaite could have formed after the replacement of any PGS precursor,

significant differences arise when attempting to balance the new distribution of Ta, as seen from the Nb/(Nb+Ta) average ratio of 0.57 for pyrochlores, compared to nearly Nb-endmember carlosbarbosaite with Nb/(Nb+Ta) that ranges from average values of 0.89 to 0.96 (samples 5031 and T4 trench, respectively). Released Ta could be partially balanced by late-formed tantite? (Ta_2O_5), alumotantite?, or Nb-free simpsonite, as ambiguously identified by Bardellli *et al*. (2019) by means of EDS analyses. These Ta-oxides occur in anhedral grains (≥50 μm) along intergranular contacts of late-formed quartz and also as rims over possible gittinsite or calciocatapleiite. Accordingly, alumotantite was described as a late, metastable phase by Voloshin *et al*. (1982); tantite is also described as late thin veinlets, lenticular segregations, or as an interstitial occurrence (Voloshin *et al.* 1983). No other Ta-rich/bearing species were found spatially related to carlosbarbosaite formation to support such Ta loss.

Bardelli *et al*. (2018) addressed some aspects of Nb-(Ta) solubility in order to explain the spatial distribution of transported carlosbarbosaite (disseminated or concentrated in fault zones) without textural evidence of *in situ* pseudomorphic replacement. Textural evidence of transported carlosbarbosaite suggests a lower *T* origin, likely supergenic. In such environments Deblonde *et al*. (2015) concluded that the solubilities of hydrated oxides like $Nb_2O_5{\cdot}nH_2O$(s) and $Ta_2O_5{\cdot}nH_2O$(s) at 25 °C increased with pH, with Ta^{5+} being less soluble than Nb^{5+} within the interval $8 \leq pH \leq 12$. Moreover, after the discovery of the first natural hexaniobate minerals, $[Nb_6O_{19}]^{8-}$ (known as the Lindqvist ion) formed at near-surface conditions, Friis & Casey (2018) provided evidence that Nb can be leached out of nearby primary minerals and easily transported as polyoxometalate ions in aqueous media, contradicting previous suppositions about Nb immobility. Friis & Casey (2018) have also shown through experimental data that the solubility of amorphous $Nb_2O_5{\cdot}nH_2O$ increases by more than four orders of magnitude in the pH range 7–12, a range found in mine waters and experimentally altered feldspathoids from the peralkaline Ilímaussaq rocks and waters from the Kola Peninsula. In the fault zone at the T4 trench we did not find any secondary species that could serve as unequivocal evidence of crystallization under alkaline conditions, however, miarolitic microcline and albite of the outer intermediate pegmatite zone were strongly dissolved and partially precipitated as a spongy skeleton of low-*T* quartz (chalcedony variety, Fig. 14a). Hydrolytic alteration of feldspars could have driven local concentrations of alkalis into solution through fluid-mineral reactions of the type:

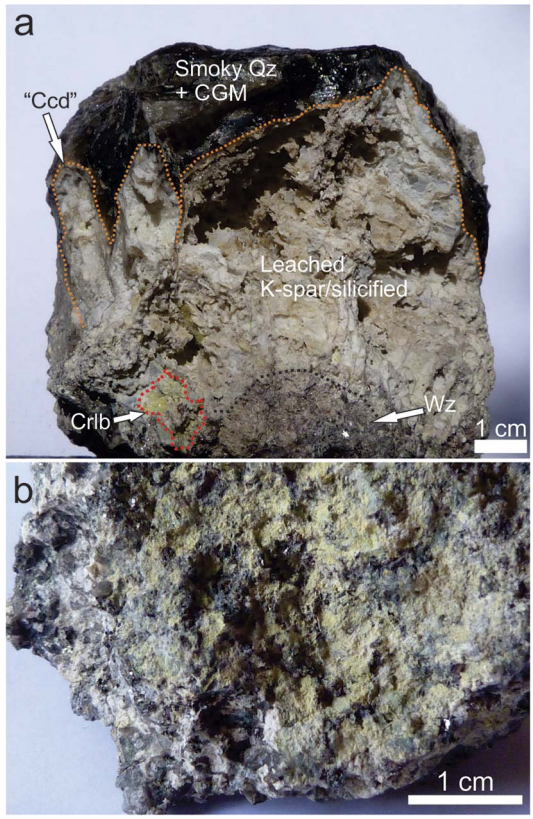

FIG. 14. (a) Fragment of miarolitic pegmatite at the T4 trench. Zonation shows the smoky quartz core which includes pseudomorphic (indigenous) carlosbarbosaite after probable CGM (shown in Fig. 7), idiomorphic, leached, and silica-replaced K-feldspar crystals lining the quartz-filled cavity, and part of the wall zone with transported carlosbarbosaite. Qz – quartz, Ccd – chalcedony, Crlb – carlosbarbosaite, Wz – wall zone. (b) Micrometer-thick yellowish coating of carlosbarbosaite on a fragment of the border-wall zone of miarolitic pegmatite, close to granite sample WP165; the left side of the sample shows graphic texture and irregularly distributed booklets of muscovite (phengite).

$$\left[KAlSi_3O_8 + 4.5H_2O + H^+ \leftrightarrow K^+ + 2Si(OH)_4 + 0.5Al_2Si_2O_5(OH)_4\right]$$

and

$$\left[NaAlSi_3O_8 + 4.5H_2O + H^+ \leftrightarrow Na^+ + 2Si(OH)_4 + 0.5Al_2Si_2O_5(OH)_4\right]$$

The products of these reactions could also explain the pseudomorphic replacement of leached microcline

crystals and cavity filling by chalcedony and clay mineral formation in the fault zone at T4 trench. Carlosbarbosaite was preferentially concentrated away from this internal feldspar leached zone, toward the wall or border zone of the pegmatite in a muscovite (phengite)-rich area (Fig. 14a–b). At this outer aureole, carlosbarbosaite crystallized under oxidizing conditions, associated with microcrystalline gypsum, Fe-oxide/hydroxide, Mn-oxides, Bi-carbonates (bismuthite), and Bi-vanadates (clinovisbanite and pucherite); both vanadates were likely derived from oxidation of pegmatitic bismuthinite while the possible source of vanadium could originate in accessory magmatic cheralite of the enclosing porphyritic facies (Bardelli *et al.* 2018). The presence of gypsum associated with transported carlosbarbosaite could be related to the fact that Ca-bearing compounds (Cl-, OH-) have been demonstrated to be efficient neutralizers, able to precipitate Nb and Ta-bearing alkaline solutions even at low concentration ranges and in a wide spectrum of pH conditions (Deblonde *et al.* 2016).

Uranium origin and mobilization

Petrographic and mineralogical studies have demonstrated that most accessory species (particularly the HFSE-rich ones) are common to both the equigranular and porphyritic granite types. These accessory species include primary late magmatic and secondary hydrothermal phases; of these, U was found hosted only in secondary hydroxycalciopyrochlore/hydroxycalciomicrolite. EDS analyses failed to detect the presence of U in any of a few probed columbite-(Fe) crystals, as it occurred with monazite-(Ce) present in micropegmatitic-miarolitic domains (*e.g.*, samples 5307b and O5-1), as well as in many tested zircon crystals (some strongly metamictic and altered, *i.e.*, sample O5-1). Thus, the enrichment of U in the equigranular granite would be somewhat proportional to the increasing amount of accessory, secondary U-bearing hydroxycalciopyrochlore/hydroxycalciomicrolite. This proportionality is strongly supported by high positive Pearson's correlation coefficients between whole-rock contents of U and Nb in the equigranular facies and, to a lesser extent, in the porphyritic facies [*i.e.*, 0.85 with data from Grosse *et al.* 2009 and Dahlquist *et al.* 2010, and 0.55 with data from Cuney (*pers. commun.*) and Bardelli *et al.* 2018]. Nevertheless, even considering the presence of accessory U-bearing hydroxycalciopyrochlore/hydroxycalciomicrolite as the main source of U in both main granite facies, the uniform areal and vertical distribution of ~160 ppm U average and of concentrations of economic significance of U in small, restricted areas (*e.g.*, up to 0.33 wt.% total U, 70% leachable), are due to the formation of low-*T* hydrothermal/supergene carlosbarbosaite. Carlosbarbosaite formed after the direct or indirect replacement of U-free columbite-(Fe) and likely after U-bearing PGS in the granites, and also after U-free Nb-bearing ilmenite and an unidentified miarolitic species, likely a CGM in the faulted miarolitic pegmatite (T4 trench). Replacement of CGM by PGS has been found in other NYF pegmatites of the world (*e.g.*, Pršek *et al.* 2010), and also marginal replacements of samarskite group minerals by PGS, particularly oxycalciopyrochlore, were described by Pieczka *et al.* (2014) in the hybrid NYF + LCT Julianna pegmatitic system at Piława Górna, SW Poland. Although not proved, this intermediate stage of the transformation CGM → PGS, prior to carlosbarbosaite formation, could have occurred in a similar fashion to how U-free monazite-(Ce) was partially replaced by P-enriched hydroxycalciopyrochlore (*i.e.*, sample 5307, pyrochlore type 2). As a matter of fact, the original findings of Arcidiácono (1974) and Arcidiácono & Bedlivy (1976a) in pegmatites of the Punilla district, Córdoba province (Argentina), showed poorly developed carlosbarbosaite as surficial, just micrometer-thick coatings on minerals of the "columbite–tantalite" series [*i.e.*, columbite-(Fe), Galliski & Černý 2006]. This might help understanding that any transformation of a CGM into a PGS would ease, favor, or speed-up carlosbarbosaite formation, otherwise only micrometer-thick replacement crusts would be formed. The incomplete pseudomorphic replacement of U-free ilmenite from the T4 trench suggests that at least part of the Nb (±Ta) was released from ilmenite, but U had to come in solution, which could also have been the case for the pseudomorphically replaced CGM, though an unknown proportion of its U content could still have been part of its original composition.

In the attempt to derive balanced chemical paths to form carlosbarbosaite from U-free CGM [*e.g.*, columbite-(Fe)], U-free ilmenite, or U-poor PGS, we obtained different unbalanced reactions, all of which require U solubilized in an aqueous reactant fluid under oxidizing conditions to form carlosbarbosaite. If columbite-(Fe) is taken as the precursor, the replacement reaction involving a U-rich aqueous fluid necessarily forms an Fe-oxide phase as by-product of carlosbarbosaite formation. This would be supported by hematite associated with carlosbarbosaite formation in the T4 trench. Similarly, if ilmenite is the precursor phase, anatase and Fe-oxides are formed as byproducts of the replacement reaction, as reported in the T4 trench (Morello 2013a, Morello & Aparicio González 2013). In the cases of carlosbarbosaite formed after the replacement of U-free, Nb(±Ta)-bearing ilmenite and of columbite-(Fe), both would essentially need U, and likely more Nb (±Ta) in the situation of ilmenite, to be sourced by such fluid. This U- and Nb-enriched fluid was active later than the replacement stage of CGM and monazite

by PGS, most likely as a residual, low-*T* hydrothermal fluid that might have collected U, Nb, and other HFSE solubilized during earlier and higher *T* reactions produced by the late-miarolitic F-Na-rich fluids that promoted albitization. In this sense, the carlosbarbosaite-forming fluid would likely represent a continuing expression of the F-Na-rich high *T* fluid grading into a lower *T*, less alkaline, and more oxidizing fluid that ultimately might have interacted with meteoric fluids. In summary, the two different carlosbarbosaite compositions found so far at La Chinchilla suggest that more different compositions could likely be found. These probable new compositions would be mostly reflected in variations of the Nb/(Nb+Ta) ratios in the octahedral site but also in variable contents of other trace or minor elements in the *Ca* and *U* sites, dependent on the different compositions of the precursor Nb-bearing phases and on the composition of the U(±Nb±Ta)-enriched fluid. It seems that the formation of carlosbarbosaite imperatively depends on the presence of pre-existing Nb-bearing oxide species, which, independently of their Nb contents, may exert a type of chemical control on the circulating U(±Nb±Ta)-bearing fluid.

Summary and Conclusions

The Lower Carboniferous A-type La Chinchilla granite pluton (~344.5 ± 1.4 Myr) is composed of two main granite facies: equigranular and porphyritic, of distinctive mineralogy and geochemistry (likely two synmagmatic bodies with independent evolutionary trends).

Their most outstanding singularity is the extraordinary amount of seriate miarolitic pegmatites from micrometric to metric sizes, dominantly hosted in the equigranular facies, which belong to the REE subclass, with close affinities with the gadolinite-fergusonite type of the NYF family.

The equigranular granite was more intensely affected by late- to post-magmatic fluid-rock interaction than the porphyritic unit. Both granite types underwent a variable, though intense, degree of muscovitization that largely transformed earlier crystallized micas of the siderophyllite–polylithionite series into Li-muscovite and muscovite (phengites).

Evidence of cavity rupture and fluid loss likely resulted from supercritical fluid overpressure in pockets. After rupture, the remaining fluids were responsible for strong albitization associated with fluorite deposition and for Nb-Ta-U-Ti redistribution and hydrothermal replacements of previous species by hydroxycalciopyrochlore + cassiterite 2 and hydroxycalciopyrochlore that evolved toward hydroxycalciomicrolite. Extremely F-rich polylithionite is paragenetically associated with the Na-F-rich replacement process. The increase of the Ta# in both secondary hydrothermal pyrochlore supergroup species and cassiterite 2 supports Nb-Ta fractionation at much lower temperatures than magmatic.

The occurrence of carlosbarbosaite at La Chinchilla would be the second confirmed worldwide; its composition can be expressed as the ideal U-bearing, strongly Nb-enriched endmember, ~two-fold enriched in Ca and with lower Nb+Ta total content than the type locality. Two main types of carlosbarbosaite were identified: indigenous and transported; the first formed after pseudomorphic replacement of Nb(±Ta)-bearing precursor species, whereas the second type crystallized within a few tens of centimeters away from the primary Nb source as coatings or vug filling precipitates. For pseudomorphic carlosbarbosaite, a circulating U^{6+} (±Nb±Ta)-bearing fluid would be essential for its formation, though some U could have also be sourced from the primary Nb-bearing replaced phase; at least in one of the studied cases a SiO_2-rich fluid was involved in its formation. Indigenous carlosbarbosaite seems to have crystallized from a low-*T* U-enriched hydrothermal fluid, likely an evolved product from the higher *T*, more alkaline, late-miarolitic F-Na-rich fluids, whereas the transported variety is likely the result of precipitation from supergene, oxidizing, and moderately alkaline fluids.

The La Chinchilla carlosbarbosaite mineralization could become a new potential U and Nb ore source, where a few favorable conditions may converge. Primarily starting with the occurrence of an appropriate amount of Nb(±Ta)-bearing accessory granite oxides, later on dissolved or replaced by low-*T* U^{6+} (±Nb±Ta)-bearing hydrothermal fluids and ultimate weathering processes, locally enhanced by fault zones.

Acknowledgments

This contribution was made possible with the aid of the National Atomic Energy Commission of Argentina (CNEA-Regional Centro, Córdoba) who supported fieldwork and allowed publication of data. We also acknowledge financial support of grants # 113/17, 411/18, and 99/19 from the SeCyT-UNC (Universidad Nacional de Córdoba, Argentina). XRD data were acquired at the INFIQC, Facultad de Ciencias Químicas (UNC); EPMA analyses were performed in the LAMARX (CONICET-UNC) facility, located in the Facultad de Matemática, Astronomía, Física y Computación, UNC (Córdoba, Argentina). L.R. Scarlatta participated in field work and sample preparation, as well as in microscopic descriptions. M.J. Espeche contributed with SEM-EDS analyses done at the LAMARX laboratory. An earlier version of the manuscript benefited from constructive comments of Bernard Bonin and the definitive version was improved with fruitful observations from two anonymous reviewers,

Editor Stephen A. Prevec, and the detailed observations of Managing Editor Mackenzie Parker.

References

Abd El-Naby, H.H. (2008) Genesis of secondary uranium minerals associated with jasperoid veins, El Erediya area, Eastern Desert, Egypt. *Mineralium Deposita* **43**, 933–944.

Alasino, P.H., Dahlquist, J.A., Galindo, C., Casquet, C., & Saavedra, J. (2010) Andalusite and Na- and Li-rich cordierite in the La Costa pluton, Sierras Pampeanas, Argentina: Textural and chemical evidence for a magmatic origin. *International Journal of Earth Sciences* **99**, 1051–1065.

Alasino, P.H., Dahlquist, J.A., Pankhurst, R.J., Galindo, C., Casquet, C., Rapela, C.W., Larrovere, M.A., & Fanning, C.M. (2012) Early Carboniferous sub- to mid-alkaline magmatism in the Eastern Sierras Pampeanas, NW Argentina: A record of crustal growth by the incorporation of mantle-derived material in an extensional setting. *Gondwana Research* **22**, 992–1008.

Anzil, P.A., Salvatore, M.A., López Pinto, M., Parra, F.J., Miyno, S.S., Scarlatta, L.R., Bello, C.F., & Álvarez, J.O. (2022) Carlosbarbosaíta como mineral de uranio en los granitos y facies tardiomagmáticas de las Sierras de Velasco. *Actas XXI Congreso Geológico Argentino*, 429–430, Puerto Madryn, Chubut, Argentina (in Spanish).

Arcidiácono, E.C. (1974) Contribución al conocimiento de columbita-tantalitas de las provincias de Córdoba y San Luis. *Revista de la Asociación Geológica Argentina* **29**, 171–184 (in Spanish).

Arcidiácono, E.C. & Bedlivy, D. (1976a) Datos preliminares sobre el hallazgo de un nuevo mineral de uranio, en Tanti (Prov. de Córdoba, R. Argentina). *Revista de la Asociación Geológica Argentina* **31**, 232–234 (in Spanish).

Arcidiácono, E.C. & Bedlivy, D. (1976b) Fases obtenidas por calentamiento de un mineral del grupo de los óxidos complejos de niobio-tantalio-titanio. *Revista de la Asociación Argentina de Mineralogía, Petrología y Sedimentología* **7**(3–4), 71–81 (in Spanish).

Armstrong, J.T. (1995) *CITZAF*: A package of correction programs for the quantitative electron microbeam X-ray analysis of thick polished material, thin films, and particles. *Microbeam Analysis* **4**, 177–200.

Atencio, D. (2013) The pyrochlore supergroup: Remarks on nomenclature – Response. *The Canadian Mineralogist* **51**, 803–804.

Atencio, D. (2021) Pyrochlore-Supergroup Minerals Nomenclature: An Update. *Frontiers in Chemistry* **9**, 713368. DOI: https://doi.org/10.3389/fchem.2021.713368

Atencio, D., Andrade, M.B., Christy, A.G., Gieré, R., & Kartashov, P.M. (2010) The pyrochlore supergroup of minerals: Nomenclature. *Canadian Mineralogist* **48**, 673–698.

Atencio, D., Roberts, A.C., Cooper, M.A., Menezes Filho, L.A. D., Coutinho, J.M.V., Stirling, J.A.R., Venance, K.E., Ball, N.A., Moffatt, E., Chaves, M.L.S.C., Brandão, P.R. G., & Romano, A.W. (2012) Carlosbarbosaite, ideally $(UO_2)_2Nb_2O_6(OH)_2{\cdot}2H_2O$, a new hydrated uranyl niobate mineral with tunnels from Jaguaraçu, Minas Gerais, Brazil: Description and crystal structure. *Mineralogical Magazine* **76**, 75–90.

Badanina, E.V., Veksler, I.V., Thomas, R., Syritso, L.F., & Trumbull, R.B. (2004) Magmatic evolution of Li-F, rare-metal granites: A case study of melt inclusions in the Khangilay complex, Eastern Transbaikalia (Russia). *Chemical Geology* **210**, 113–133.

Badanina, E.V., Syritso, L.F., Volkova, E.V., Thomas, R., & Trumbull, R.B. (2010) Composition of Li-F granite melt and its evolution during the formation of the ore-bearing Orlovka Massif in Eastern Transbaikalia. *Petrology* **18**(2),131–157.

Bardelli, F.M. (2014) *Caracterización de los sistemas hidrotermales y su relación con la mineralización de uranio en el granito La Chinchilla, Sierra de Velasco, La Rioja.* Graduate thesis National University of Córdoba, Córdoba, Argentina (in Spanish).

Bardelli, F.M., Parra, F.J., & Lira, R. (2018) Minerales accesorios y procesos de alteración del granito La Chinchilla, sierra de Velasco, La Rioja: aspectos mineralógicos y geoquímicos en su relación con mineralización uranífera. *Revista de la Asociación Geológica Argentina* **75**(1), 134–151 (in Spanish).

Beus, A.A., Severov, E.A., Sitnin, A.A., & Subbotin, K.D. (1962) *Albitized and Greisenized Granite (Apogranite)*. Izvestiya Akademii SSSR, Moscow, Russia (in Russian).

Bonazzi, P., Bindi, L., Zoppi, M., Capitani, G.C., & Olmi, F. (2006) Single-crystal diffraction and transmission electron microscopy studies of "silicified" pyrochlore from Narssârssuk, Julianehaab district, Greenland. *American Mineralogist* **9**, 794–801.

Borodulin, G.P., Chevychelov, V.Yu, & Zaraysky, G.P. (2009) Experimental study of partitioning of tantalum, niobium, manganese, and fluorine between aqueous fluoride fluid and granitic and alkaline melts. *Doklady Earth Sciences* **427**(5), 868–873.

Candela, P.A. (1997) A review of shallow, ore-related granites: textures, volatiles, and ore metals. *Journal of Petrology* **38**(12), 1619–1633.

Candela, P.A. & Blevin, P.L. (1995) Do some miarolitic granites preserve evidence of magmatic volatile phase permeability? *Economic Geology* **90**(8), 2310–2316.

Černý, P. & Ercit, T.S. (1985) Some recent advances in the mineralogy and geochemistry of Nband Ta in rare-element granitic pegmatites. *Bulletin de Minéralogie* **108**, 499–532.

Černý, P. & Ercit, T.S. (1989) Mineralogy of niobium and tantalum: Crystal chemical relationships, paragenetic aspects and their economic implications. *In* Lanthanides, Tantalum and Niobium (P. Möller, P. Černý, and F. Saupé, eds.). Springer-Verlag, Berlin, Germany (27–79).

Chevychelov, V.Yu, Borodulin, G.P., & Zaraisky, G.P. (2010) Solubility of columbite, $(Mn,Fe)(Nb,Ta)_2O_6$, in granitoid and alkaline melts at 650–850 °C and 30–400 MPa: An experimental investigation. *Geochemistry International* **48**, 456–464.

Chipera, S.J. & Bish, D.L. (2002) Thermal evolution of fluorine from smectite and kaolinite. *Clays and Clay Minerals* **50**(1), 38–46.

Christy, A.G. & Atencio, D. (2013) Clarification of status of species in the pyrochlore supergroup. *Mineralogical Magazine* **77** (1), 13–20.

Dahlquist, J.A., Alasino, P.H., Eby, G.N., Galindo, C., & Casquet, C. (2010) Fault-controlled Carboniferous A-type magmatism in the proto-Andean foreland (Sierras Pampeanas, Argentina): Geochemical constraints and petrogenesis. *Lithos* **115**, 65–81.

Dahlquist, J.A., Pankhurst, R.J., Gaschnig, R.M., Rapela, C.W., Casquet, C., Alasino, P.H., Galindo, C., & Baldo, E.G. (2013) Hf and Nd isotopes in Early Ordovician to Early Carboniferous granites as monitors of crustal growth in the Proto-Andean margin of Gondwana. *Gondwana Research* **23**, 1671–1630.

De Ignacio, C., Muñoz, M., & Sagredo, J. (2012) Carbonatites and associated nephelinites from São Vicente, Cape Verde Islands. *Mineralogical Magazine* **76**, 2, 311–355.

Deblonde, G.J.-P., Chagnes, A., Bélair, S., & Cote, G. (2015) Solubility of niobium (V) and tantalum (V) under mild alkaline conditions. *Hydrometallurgy* **156**, 99–106.

Deblonde, G.J.-P., Chagnes, A., Weigel, V., & Cote, G. (2016) Direct precipitation of niobium and tantalum from alkaline solutions using calcium-bearing reagents. *Hydrometallurgy* **165**, 345–350.

Deditius, A.P., (Skomurski) Smith, F.N., Utsunomiya, S., & Ewing, R.C. (2015) Role of vein-phases in nanoscale sequestration of U, Nb, Ti, and Pb during the alteration of pyrochlore. *Geochimica et Cosmochimica Acta* **150**, 226–252.

Demartis, M., Melgarejo, J.C., Colombo, F., Alfonso, P., Coniglio, J.E., Pinotti, L.P., & D'eramo, F.J. (2014) Extreme F activities in late pegmatitic events as a key factor for LILE and HFSE enrichment: The Ángel pegmatite, Central Argentina. *The Canadian Mineralogist* **52**(2), 247–269.

Di, H., Shao, Y.-J., Jiang, S.-Y., Brzozowski, M.J., Wang, Z., & Xiong, Y.-Q. (2023) Identifying superimposed W-Sn mineralization events using cassiterite microtextures, trace-element chemistry, and geochronology. *Ore Geology Reviews* **153**, 105281.

Dumanska-Slowik, M.A., Pieczka, A., Tempesta, G., Olejniczak, Z., & Heflik, W. (2014) "Silicified" pyrochlore from nepheline syenite (mariupolite) of the Mariupol Massif, SE Ukraine: A new insight into the role of silicon in the pyrochlore structure. *American Mineralogist* **99**(10), 2008–2017.

Feng, Y., Liang, T., Yang, X., Zhang, Z., & Wang, Y. (2019) Chemical evolution of Nb-Ta oxides and cassiterite in phosphorus-rich albite-spodumene pegmatites in the Kangxiwa–Dahongliutan pegmatite field, Western Kunlun Orogen, China. *Minerals* **9**, 166. DOI: https://doi.org/10.3390/min9030166

Foord, E.E., Soregaroli, A.E., & Gordon, H.M. (1999) The Zapot pegmatite. Mineral County, Nevada. *Mineralogical Record* **30**, 277–292.

Friis, H. & Casey, W.H. (2018) Niobium is highly mobile as a polyoxometalate ion during natural weathering. *The Canadian Mineralogist* **56**, 1–8.

Galliski, M.Á. & Černý, P. (2006) Geochemistry and structural state of columbite-group minerals from granitic pegmatites of the Pampean Ranges, Argentina. *The Canadian Mineralogist* **44**, 645–666.

Galliski, M.Á., Márquez-Zavalía, M.F., Černý, P., Martínez, V.A., & Chapman, R. (2008) The Ta-Nb-Sn-Ti oxide-mineral paragenesis from La Viquita, a spodumene-bearing rare-element granitic pegmatite, San Luis, Argentina. *The Canadian Mineralogist* **46**(2), 379–393.

Geisler, T., Berndt, J., Meyer, H.-W., Pollok, K., & Putnis, A. (2004) Low-temperature aqueous alteration of crystalline pyrochlore: Correspondence between nature and experiment. *Mineralogical Magazine* **68**, 905–922.

Goldsmith, J.R. & Laves, F. (1954) The microcline-sanidine stability relations. *Geochimica et Cosmochimica Acta* **5**, 1–19.

Grosse, P. (2007) *Los granitos porfíricos y orbiculares del sector centro-oriental de la Sierra de Velasco: génesis y significación regional.* PhD Dissertation, National University of Córdoba, Córdoba, Argentina (in Spanish).

Grosse, P. & Sardi, F.G. (2005) Geología de los granitos Huaco y Sanagasta, sector centro-oriental de la Sierra de Velasco, La Rioja. *In* Simposio Bodenbender (F.G. Aceñolaza, G. Aceñolaza, M. Hünicken, J.N. Ross, and A.J. Toselli, eds.). Serie Correlación Geológica 19, San Miguel de Tucumán, Argentina (221–238) (in Spanish).

Grosse, P., Larrovere, M., De La Rosa, J.D., & Castro, A. (2005) Petrología y origen del stock La Chinchilla, Sierra de Velasco, La Rioja (Argentina). 16th Congreso Geológico Argentino, La Plata, Argentina, 533–538 (in Spanish).

Grosse, P., Rossi, J.N., Sardi, F.G., & Toselli, A. (2006) Química mineral de los granitos Sanagasta, Huaco y La Chinchilla, Sierra de Velasco, La Rioja, Argentina. VIII Congreso de Mineralogía y Metalogenia, Actas, 381–388 (in Spanish).

Grosse, P., Söllner, F., Báez, M., Toselli, A., Rossi, J., & De La Rosa, J.D. (2009) Lower Carboniferous post-orogenic granites in central-eastern Sierra de Velasco, Sierras Pampeanas, Argentina: U-Pb monazite geochronology, geochemistry and Sr–Nd isotopes. *International Journal of Earth Sciences* **98**, 1001–1025.

Hogarth, D.D. (1977) Classification and nomenclature of the pyrochlore group. *American Mineralogist* **62**, 403–410.

Janeczek, J. (2007) Intragranitic pegmatites of the Strzegom–Sobótka massif – An overview. Granitoids in Poland. *American Mineralogist Monograph* **1**, 193–201.

Jiang, N., Sun, S., Chu, X., Mizuta, T., & Ishiyama, D. (2003) Mobilization and enrichment of high-field strength elements during late- and post-magmatic processes in the Shuiquangou syenitic complex, Northern China. *Chemical Geology* **200**, 117–128.

Jiang, S.Y., Wang, R.C., Xu, X.S., & Zhao, K.D. (2005) Mobility of high field strength elements (HFSE) in magmatic-, metamorphic-, and submarine-hydrothermal systems. *Physics and Chemistry of the Earth* **30**(17–18), 1020–1029. DOI: https://doi.org/10.1016/j.pce.2004.11.004

Keppler, H. (1993) Influence of fluorine on the enrichment of high field strength trace elements in granitic rocks. *Contributions to Mineralogy and Petrology* **114**, 479–488.

Kinnaird, J.A. (1984) Contrasting styles of Sn-Nb-Ta-Zn mineralization in Nigeria. *Journal of African Earth Sciences* **2**(2), 81–90.

Laurs, B.M., Dilles, J.H., Wairrach, Y., Kausar, A.B., & Snee, L. (1998) Geological setting and petrogenesis of symmetrically zoned, miarolitic granitic pegmatites at Stak Nala, Nanga Parbat-Haramosh Massif, Northern Pakistan. *The Canadian Mineralogist* **36**, 1–47.

Linnen, R.L., Van Lichtervelde, M., & Černý, P. (2012) Granitic pegmatites as sources of strategic metals. *Elements* **8**, 275–280.

Lira, R., Parra, F., Bardelli, F.M., Galliski, M.A., & Scarlatta, L.R. (2015) Amazonite from miarolitic NYF pegmatites and primary accessory minerals of the A-type La Chinchilla granite, Sierra de Velasco, La Rioja province, Argentina. *7th International Symposium on Granitic Pegmatites*, PEG 2015, Książ, Poland, 40–41.

Llorens González, T., García Polonio, F., López Moro, F.J., Fernández Fernández, A., Sanz Contreras, J.L., & Moro Benito, M.C. (2017) Tin-tantalum-niobium mineralization in the Penouta deposit (NW Spain): Textural features and mineral chemistry to unravel the genesis and evolution of cassiterite and columbite group minerals in a peraluminous system. *Ore Geology Reviews* **8**, 79–95.

López, L., Álvarez, J., Parra, F., Anzil, P., Bello, C., Ceballos, E., Salvatore, M., Scarlatta, L., Miyno, S., Felkai, E., Ferreyra, P., Zelaya, A., Cuney, M., Mercadier, J., Hanly, A., & Lira, R. (2020) Granite-related uranium deposits in Argentina. Geological context and new metallogenetic studies. *In* Geochemical and Mineralogical Characterization of Uranium and Thorium Deposits, Final Report of a Coordinated Research Project, IAEA-TECDOC-1929, IAEA, Vienna (11–44).

Lukyanova, E.V., Akinfiev, N.N., Zotov, A.V., Rass, I.T., Kotova, N.P., & Korzhinskaya V.S. (2017) Niobium in hydrothermal systems related to alkali granites: Thermodynamic description of hydroxo and hydroxofluoride complexes. *Geology of Ore Deposits* **59**(4), 305–314.

Lumpkin, G.R. & Ewing, R.C. (1995) Geochemical alteration of pyrochlore group minerals: pyrochlore subgroup. *American Mineralogist* **80**(7–8), 732–743.

Macchioli Grande, M., Alasino, P.H., Rocher, S., Larrovere, M.A., & Dahlquist, J.A. (2015) Asymmetric textural and structural patterns of a granitic body emplaced at shallow levels: The La Chinchilla pluton, northwestern Argentina. *Journal of South American Earth Sciences* **64**, 58–68.

Macchioli Grande, M., Alasino, P.H., Rocher, S., Larrovere, M.A., Uran, G.M., Reinoso Carbonell, V., & Moreno, G. (2019) Thermal evolution of upper crustal magmatic systems from the Sierra de Velasco, NW Argentina. *Journal of Structural Geology* **118**, 1–20.

Mackay, D.A.R. & Simandl, G.J. (2015) Pyrochlore and columbite-tantalite as indicator minerals for specialty metal deposits. *Geochemistry: Exploration, Environment, Analysis* **15**, 167–178. DOI: https://doi.org/10.1144/geochem2014-289

Manning, D.A.C. (1981) The effect of fluorine on liquidus phase relationships in the system Qz-Ab-Or with excess water at 1 kbar. *Contributions to Mineralogy and Petrology* **76**, 206–215.

Martin, R.F., De Vito, C., & Pezzotta, F. (2008) Why is amazonitic K-feldspar an earmark of NYF-type granitic pegmatites? Clues from hybrid pegmatites in Madagascar. *American Mineralogist* **93**, 263–269.

Matyszczak, W. (2018) Liandratite from Karkonosze pegmatites, Sudetes, Southwestern Poland. *Mineralogy and Petrology* **112**, 357–370. DOI: https://doi.org/10.1007/s00710-017-0537-8

McGregor, J.R. & Ferguson, R.B. (1989) Characterization of phases and twins in alkali feldspars by the X-ray precession technique. *The Canadian Mineralogist* **27**, 457–482.

Mokhov, A.V., Kartashov, P.M., Bogatikov, O.A., Ashikhmina, N.A., Magazina, L.O., & Koporulina, E.V. (2008) Fluorite, hatchettolite, calcium sulfate, and bastnasite-(Ce) in the lunar regolith from Mare Crisium. *Doklady Earth Sciences* **422**(7), 1178–1180.

Möller, P., Dulski, P., Szacki, W., Malow, G., & Riedel, E. (1988) Substitution of tin in cassiterite by tantalum,

niobium, tungsten, iron and manganese. *Geochimica et Cosmochimica Acta* **52**, 1497–1503.

Morello, O. (2013a) Mineral de U-Nb-Ta en el Granito La Chinchilla Sierra de Velasco, La Rioja. 10th Congreso Argentino de Geología Económica, Actas, San Juan, Argentina, 259–262 (in Spanish).

Morello, O. (2013b) Nuevo hallazgo del óxido de uranio-niobio-tantalio en Argentina. I Reunión Latinoamericana de Cristalografía, IX Reunión Anual de la Asociación Argentina de Cristalografía, Actas, p. 1 (in Spanish).

Morello, O. & Aparicio González, P. (2013) Mineralización de uranio en la Sierra de Velazco, La Rioja. *Revista de la Asociación Geológica Argentina* **70**, 335–340 (in Spanish).

Müller, A., Spratt, J., Thomas, R., Williamson, B.J., & Seltmann, R. (2018) Alkali-F-rich albite zones in evolved NYF pegmatites: The product of melt–melt immiscibility. *The Canadian Mineralogist* **56**, 657–687. DOI: https://doi.org/10.3749/canmin.1700087

Nasraoui, M. & Bilal, E. (2000) Pyrochlores from the Lueshe carbonatite complex (Democratic Republic of Congo): A geochemical record of different alteration stages. *Journal of Asian Earth Sciences* **18**(2), 237–251.

Nasraoui, M., Bilal, E., & Gibert, R. (1999) Fresh and weathered pyrochlore studies by Fourier transform infrared spectroscopy coupled with thermal analysis. *Mineralogical Magazine* **63**(4), 567–578.

Pal, D.C., Mishra, B., & Bernhardt, H.-J. (2007) Mineralogy and geochemistry of pegmatites-hosted Sn-, Ta-Nb-, and Zr-Hf-bearing minerals from the southeastern part of the Bastar-Malkangiri Pegmatites Belt, Central India. *Ore Geology Reviews* **30**, 30–55.

Pankhurst, R., Rapela, C., & Fanning, C. (2000) Age and origin of coeval TTG, I- and S- type granites in the Famatinian Belt of NW Argentina. *Transactions of the Royal Society of Edinburgh, Earth Sciences* **91**, 151–168.

Parra, F.J., Blasón, R., Álvarez, J.O., Zarco Ambrosio, J.J., & Bello, C. (2011) Estimación de recursos uraníferos potenciales en el stock La Chinchilla, Sierra de Velasco, provincia de La Rioja. 18th Congreso Geológico Argentino, Neuquén, Argenina, 959–960 (in Spanish).

Peretyazhko, I.S. (2010) Genesis of mineralized cavities (miaroles) in granitic pegmatites and granites. *Petrology* **18**(2), 183–208.

Peretyazhko, I.S. & Zagorsky, V.Ye. (2002) The influence of H_3BO_3 on fluid pressure in granitic pegmatite miaroles: A computation of isochores and the density of boric acid solutions. *Doklady Earth Sciences* **383A**(3), 340–345. Translated from *Doklady Akademii Nauk* **383**(6), 812–817.

Peretyazhko, I.S., Zagorsky, V.Ye, Smirnov, S.Z., & Mikhailov, M.Y. (2004) Conditions of pocket formation in the Oktyabrskaya tourmaline-rich gem pegmatite (the Malkhan field, Central Transbaikalia, Russia). *Chemical Geology* **210**, 91–111.

Pieczka, A., Szuszkiewicz, A., Szełęg, E., Ilnicki, S., Nejbert, K., & Turniak K. (2014) Samarskite-group minerals and alteration products: An example from the Julianna pegmatitic system, Piława Górna, SW Poland. *The Canadian Mineralogist* **52**, 303–319.

Pršek, J., Majka, J., Uher, P., & Chudík, P. (2010) Niobium-tantalum minerals in the Skoddefjellet NYF granitic pegmatite, Svalbard Archipelago, Norway: Primary versus secondary assemblage. *Neues Jahrbuch für Mineralogie – Abhandlungen* **187**(3), 235–248.

Rickers, K., Thomas, R., & Heinrich, W. (2006) The behavior of trace elements during the chemical evolution of the H_2O-, B-, and F-rich granite–pegmatite–hydrothermal system at Ehrenfriedersdorf, Germany: A SXRF study of melt and fluid inclusions. *Mineralium Deposita* **41**, 229–245. DOI: https://doi.org/10.1007/s00126-006-0057-7

Salvatore, M., Parra, F.J., Sánchez, D.L., Álvarez, J.O., Bello, C., & Zarco Ambrosio, J.J. (2013) Caracterización litogeoquímica del granito La Chinchilla y su relación con el uranio, Sierra de Velasco, Provincia de La Rioja. *Revista de la Asociación Geológica Argentina* **70**(3), 341–350 (in Spanish).

Sardi, F. & Heimann, A. (2014) Pegmatitic beryl as indicator of melt evolution: Example from the Velasco district, Pampeana Pegmatite Province, Argentina, and review of worldwide occurrences. *The Canadian Mineralogist* **52**(5), 809–836.

Sardi, F.G., Heimann, A., & Grosse, P. (2013) Estudio composicional preliminar del berilo del granito La Chinchilla, Sierra de Velasco, Argentina. 11th Congreso de Mineralogía y Metalogenia, Actas, San Juan, Argentina, 145–146 (in Spanish).

Sardi, F., Heimann, A., & Grosse, P. (2016) Non-pegmatitic beryl related to Carboniferous granitic magmatism, Velasco Range, Pampean Province, NW Argentina. *Andean Geology* **43**, 86–104.

Saulnier, M.E. & Morello, O. (2002) Mineral de U-Ta-Nb en los granitos San Ignacio-Cumbre de los Pinos, Catamarca-Tucumán. 6th Congreso de Mineralogía y Metalogenia, Actas, Buenos Aires, Argentina, 421–424 (in Spanish).

Schwartz, M.O. (1992) Geochemical criteria for distinguishing magmatic and metasomatic albite-enrichment in granitoids – Examples from the Ta-Li granite Yichun (China) and the Sn-W deposit Tikus (Indonesia). *Mineralium Deposita* **27**, 101–108.

Shapovalov, Y.B., Chevychelov, V.Y., Korzhinskaya, V.S., Kotova, N.P., Redkin, A.F., & Konyshev, A.A. (2019) Physical and chemical parameters of processes producing rare-metal deposits in granitoid systems with fluorine: Experimental data. *Petrology* **27**(6), 567–584. Translated from *Petrologiya* **27**(6), 617–637 (2019).

Starikova, A.E., Bazarova, E.P., Savel'eva, V.B., Sklyarov, E.V., Khromova, E.A., & Kanakin, S.V. (2019) Pyrochlore-group minerals in the granite-hosted Katugin rare-metal deposit, Transbaikalia, Russia. *Minerals* **9**(8), 490. DOI: https://doi.org/10.3390/min9080490

Thomas, R. & Davidson, P. (2013) The missing link between granites and granitic pegmatites. *Journal of Geosciences* **58**, 183–200.

Thomas, R. & Davidson, P. (2014) Liquid immiscibility – Important processes during pegmatite formation. Pan-American Current Research on Fluid Inclusions (PACROFI-XII), U.S. Geological Survey and Colorado State University, Abstract Volume, 52–53.

Thomas, R. & Davidson, P. (2016) Origin of miarolitic pegmatites in the Königshain granite/Lusatia. *Lithos* **260**, 225–241.

Thomas, J., Jr., Glass, H.D., White, W.A., & Trandel, R.M. (1977) Fluorine content of clay minerals and argillaceous earth materials. *Clays and Clay Minerals* **25**, 278–284.

Thomas, R., Förster, H.-J., Rickers, K., & Webster, J.D. (2005) Formation of extremely F-rich hydrous melt fractions and hydrothermal fluids during differentiation of highly evolved tin-granite magmas: A melt/fluid-inclusion study. *Contributions to Mineralogy and Petrology* **148**, 582–601.

Thomas, R., Davidson, P., Rhede, D., & Leh, M. (2009) The miarolitic pegmatites from the Königshain: A contribution to understanding the genesis of pegmatites. *Contributions to Mineralogy and Petrology* **157**, 505–523.

Thomas, R., Webster, J.D., Rhede, D., Seifert, W., Rickers, K., Förster, H.-J., Heinrich, W., & Davidson, P. (2006) The transition from peraluminous to peralkaline granitic melts: Evidence from melt inclusions and accessory minerals. *Lithos* **91**, 137–149.

Tischendorf, G., Förster, H.-J., Gottesmann, B., & Rieder, M. (2007) True and brittle micas: Composition and solid-solution series. *Mineralogical Magazine* **71**(3), 285–320.

Tischendorf, G., Rieder, M., Förster, H.-J., Gottesmann, B., & Guidotti, Ch.V. (2004) A new graphical presentation and subdivision of potassium micas. *Mineralogical Magazine* **68**(4), 649–667.

Toselli, A.J., Durand, F.R., Rossi de Toselli, J.N., & Saavedra, J. (1996) Esquema de evolución geotectónica y magmática eopaleozoica del Sistema de Famatina y sectores de Sierras Pampeanas. 13th Congreso Geológico Argentino and 3rd Congreso de Exploración de Hidrocarburos, Actas 5, Buenos Aires, Argentina, 443–462 (in Spanish).

Voloshin, A.V., Men'shikov, Yu.P., & Pakhomovskiy, Y.A. (1982) Alumotantite and natrotantite, new tantalum minerals in granitic pegmatites. *International Geology Review* **24**(7), 835–842. DOI: https://doi.org/10.1080/00206818209449623

Voloshin, A.V., Pakhomovskii, Y.A., & Perlina, G.A. (1983) Tantite Ta_2O_5 – A new mineral from granitic pegmatites of the Kola Peninsula. *Mineralogiceskij Zhurnal* **5**(3), 90–93.

Wall, F., Williams, C.T., Woolley, A.R., & Nasraoui, M. (1996) Pyrochlore from weathered carbonatite at Lueshe, Zaire. *Mineralogical Magazine* **60**(402), 731–750.

Williams, C.T., Wall, F., Woolley, A.R., & Phillipo, S. (1997) Compositional variation in pyrochlore from the Bingo carbonatite, Zaïre. *Journal of African Earth Sciences* **25**(1), 137–145.

Zaitsev, A.N., Williams, C.T., Wall, F., & Zolotarev, A.A. (2012) Evolution of chemical composition of pyrochlore group minerals from phoscorites and carbonatites of the Khibina alkaline massif. *Geology of Ore Deposits* **54**(7), 503–515.

Zaraisky, G.P., Korzhinskaya, V., & Kotova, N. (2010) Studies of Ta_2O_5 and columbite–tantalite solubility in fluoride solutions from 300 to 550 °C and 50 to 100 MPa. *Mineralogy and Petrology* **99**, 287–300. DOI: https://doi.org/10.1007/s00710-010-0112-z

Received January 26, 2023. Revised manuscript accepted June 5, 2023.

This manuscript was handled by Associate Editor Ru Cheng Wang and Editor Steve Prevec.